

NO-A184 881

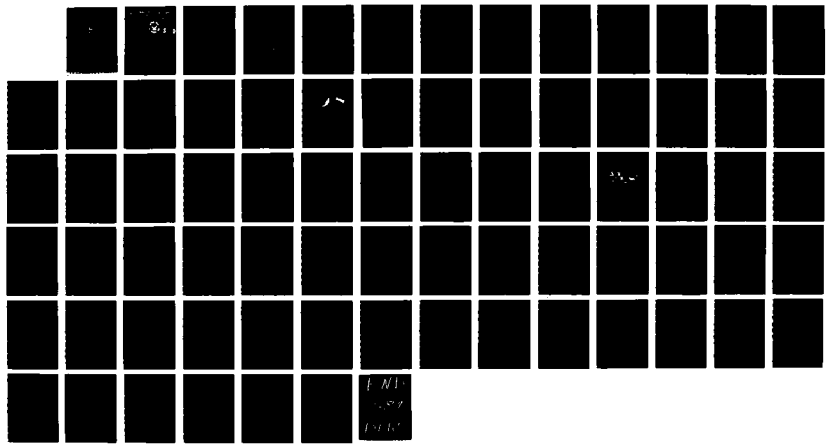
ESTIMATION OF MARINE BOUNDARY LAYER DEPTH AND RELATIVE HUMIDITY WITH MULTISPECTRAL SATELLITE MEASUREMENTS(U)
NAVAL POSTGRADUATE SCHOOL MONTEREY CA R J KREN JUN 87

1/1

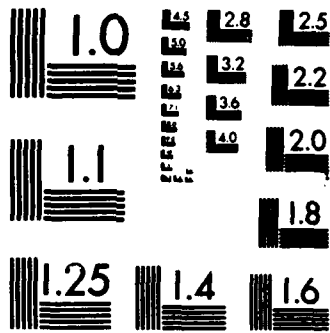
UNCLASSIFIED

F/G 4/2

NL



101-
187
1-11



MICROCOPY RESOLUTION TEST CHART
NATIONAL BUREAU OF STANDARDS-1963-A

AD-A184 881

2

NAVAL POSTGRADUATE SCHOOL Monterey, California

DTIC FILE COPY



DTIC
ELECTE
OCT 07 1987
S D
D

THESIS

ESTIMATION OF MARINE BOUNDARY LAYER
DEPTH
AND RELATIVE HUMIDITY
WITH MULTISPECTRAL SATELLITE
MEASUREMENTS

by

Richard J. Kren

June 1987

Thesis Advisor

Philip A. Durkee

Approved for public release; distribution is unlimited.

87 9 25 140

87 9 25 140

REPORT DOCUMENTATION PAGE

1a REPORT SECURITY CLASSIFICATION UNCLASSIFIED		1b RESTRICTIVE MARKINGS	
2a SECURITY CLASSIFICATION AUTHORITY		3 DISTRIBUTION/AVAILABILITY OF REPORT Approved for public release; distribution is unlimited.	
2b DECLASSIFICATION/DOWNGRADING SCHEDULE		5 MONITORING ORGANIZATION REPORT NUMBER(S)	
4 PERFORMING ORGANIZATION REPORT NUMBER(S)		7a NAME OF MONITORING ORGANIZATION Naval Postgraduate School	
6a NAME OF PERFORMING ORGANIZATION Naval Postgraduate School	6b OFFICE SYMBOL (if applicable) 63	7b ADDRESS (City, State, and ZIP Code) Monterey, California 93943-5000	
6c ADDRESS (City, State, and ZIP Code) Monterey, California 93943-5000		9 PROCUREMENT INSTRUMENT IDENTIFICATION NUMBER	
8a NAME OF FUNDING/SPONSORING ORGANIZATION	8b OFFICE SYMBOL (if applicable)	10 SOURCE OF FUNDING NUMBERS	
8c ADDRESS (City, State, and ZIP Code)		PROGRAM ELEMENT NO	PROJECT NO
		TASK NO	WORK UNIT ACCESSION NO
11 TITLE (Include Security Classification) ESTIMATION OF MARINE BOUNDARY LAYER DEPTH AND RELATIVE HUMIDITY WITH MULTISPECTRAL SATELLITE MEASUREMENTS - UNCLAS.			
12 PERSONAL AUTHOR(S) Kren, Richard J.			
13a TYPE OF REPORT Master's Thesis	13b TIME COVERED FROM _____ TO _____	14 DATE OF REPORT (Year Month Day) 1987 June	15 PAGE COUNT 74
16 SUPPLEMENTARY NOTATION			
17 COSAT CODES		18 SUBJECT TERMS (Continue on reverse if necessary and identify by block number)	
FIELD	GROUP	SUB GROUP	
		Satellite, Boundary Layer, Remote Sensing	
<p>This study presents a technique for estimating marine boundary layer depth and relative humidity structure from satellite inferred measurements of aerosol optical depth, total water vapor and sea surface temperature. The data originates from radiance measurements by channels 1, 4 and 5 of NOAA's AVHRR instrument. The technique assumes that the atmospheric optical depth and total water vapor are primarily confined within the boundary layer, and that the layer is well-mixed. These inputs are combined through the relative humidity dependent variables of extinction and vapor density. Relative humidity is parameterized as an increasing linear function with height, resulting in an equation for the near surface relative humidity. This equation is solved, enabling estimation of boundary layer depth and humidity structure. The technique is iterative in nature, requiring 5 to 10 iterations for convergence.</p>			
20 DISTRIBUTION AVAILABILITY OF ABSTRACT <input checked="" type="checkbox"/> UNCLASSIFIED UNLIMITED <input type="checkbox"/> SAME AS RPT <input type="checkbox"/> OTC USERS		21 ABSTRACT SECURITY CLASSIFICATION UNCLASSIFIED	
22a NAME OF RESPONSIBLE INDIVIDUAL Phillip A. Durkee		22b TELEPHONE (Include Area Code) (408)-646-2044	22c OFFICE SYMBOL 63De

Approved for public release; distribution is unlimited.

Estimation of Marine Boundary Layer Depth
and Relative Humidity
with Multispectral Satellite Measurements

by

Richard J. Kren
Lieutenant, United States Navy
B.S., Parks College of St. Louis University, 1980

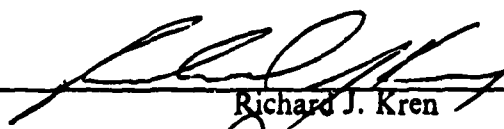
Submitted in partial fulfillment of the
requirements for the degree of

MASTER OF SCIENCE IN METEOROLOGY AND OCEANOGRAPHY

from the

NAVAL POSTGRADUATE SCHOOL
June 1987

Author:



Richard J. Kren

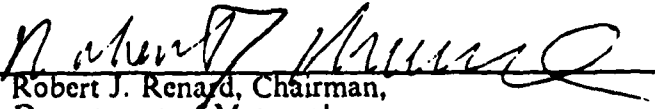
Approved by:



Philip A. Darkce, Thesis Advisor



Carlyle H. Wash, Second Reader



Robert J. Renard, Chairman,
Department of Meteorology



Gordon E. Schacher,
Dean of Science and Engineering

ABSTRACT

This study presents a technique for estimating marine boundary layer depth and relative humidity structure from satellite inferred measurements of aerosol optical depth, total water vapor and sea-surface temperature. The data originate from radiance measurements by channels 1, 4 and 5 of NOAA's AVHRR instrument. The technique assumes that the atmospheric optical depth and total water vapor are primarily confined within the boundary layer, and that the layer is well-mixed. These inputs are combined through the relative humidity dependent variables of extinction and vapor density. Relative humidity is parameterized as an increasing linear function with height, resulting in an equation for the near-surface relative humidity. This equation is solved, enabling estimation of boundary layer depth and humidity structure. The technique is iterative in nature, requiring 5 to 10 iterations for convergence.



Accession For	
NTIS CRA&I	<input checked="" type="checkbox"/>
DTIC TAB	<input type="checkbox"/>
Unannounced	<input type="checkbox"/>
Justification	
By _____	
Distribution/	
Availability Codes	
Dist	Availability of Special
A-1	

TABLE OF CONTENTS

I.	INTRODUCTION	10
II.	THEORETICAL BACKGROUND	13
	A. MEASUREMENT OF OPTICAL DEPTH	13
	1. Radiative Transfer to Estimate Optical Depth	13
	2. Effect of Radiometric Quantities on Optical Depth	16
	3. Optical Depth and Relative Humidity	21
	B. MEASUREMENT OF WATER VAPOR	24
	1. Radiative Transfer and Satellite Techniques to Recover Water Vapor	26
	2. Total Water Vapor and Relative Humidity	29
	C. MEASUREMENT OF SEA-SURFACE TEMPERATURE	31
	D. CHARACTERISTICS OF THE MABL	31
	1. Processes within the MABL	31
	2. Relationship Between Variables within the Well-Mixed MABL	32
	E. TECHNIQUE ASSUMPTIONS	34
	1. Validity of Optical Depth within the MABL	34
	2. Validity of Total Water Vapor within the MABL	34
	3. Validity of Well-Mixed MABL	36
III.	ESTIMATION OF MABL DEPTH AND RELATIVE HUMIDITY	38
	A. RELATIVE HUMIDITY PARAMETERIZATION	38
	B. INTEGRATED OPTICAL DEPTH AND WATER VAPOR	39
	C. NEAR-SURFACE RELATIVE HUMIDITY AND MABL THICKNESS	39
	D. THE ITERATIVE PROCESS	43
	1. Saturation Vapor Density	44

	2. C - Relative Humidity Variable	45
IV.	TECHNIQUE RESPONSE TO A SIMULATED BOUNDARY LAYER	47
	A. MODEL STRUCTURE	47
	B. TECHNIQUE PERFORMANCE IN A SIMULATED MABL	48
	1. Variations in Layer Depths	49
	2. Variations in Surface Relative Humidity	49
	C. TECHNIQUE SYSTEMATIC ERRORS	55
	D. RELATIONSHIP BETWEEN SURFACE RELATIVE HUMIDITY AND MABL DEPTH	56
V.	SENSITIVITY TO UNCERTAINTY IN MEASUREMENTS	59
	A. RESULTS OF SENSITIVITY STUDIES	59
	1. Uncertainty in Observed Water Vapor	59
	2. Uncertainty in Observed Optical Depth	61
	3. Uncertainty in Observed Sea-Surface Temperatures	62
	4. Uncertainty in Observed Sea-Level Pressure	62
	B. COMPARISON OF ERRORS IN INPUT VALUES	63
VI.	CONCLUSIONS AND RECOMMENDATIONS	66
	LIST OF REFERENCES	68
	INITIAL DISTRIBUTION LIST	71

LIST OF TABLES

1. EXTINCTION COEFFICIENT VERSUS RELATIVE HUMIDITY	24
2. DEVIATION BETWEEN TECHNIQUE AND MODEL LAYER DEPTH	56
3. EFFECT OF VARIATIONS IN w ON SURFACE HUMIDITY AND MABL DEPTH	60
4. EFFECT OF VARIATIONS IN τ ON SURFACE HUMIDITY AND MABL DEPTH	61
5. EFFECT OF VARIATIONS IN SST ON SURFACE HUMIDITY AND MABL DEPTH	63

LIST OF FIGURES

2.1	Favorable viewing geometries for atmospheric turbidity with satellite zenith angles of 12.5° (left), and 57.5° (right). (Koepke and Quenzel, 1979)	17
2.2	The terms of the extinction formulation as a function of particle radius from Durkee (1984). See text for a more complete description of panels a,b,c and d.	19
2.3	Upwelling radiance variation for particle size variations as a result of wind speed variations. (Durkee, 1984)	20
2.4	Single-scattering phase function as a function of relative humidity. (Durkee, 1984)	22
2.5	Variation in upwelling radiance as a function of relative humidity from Durkee (1984)	23
2.6	Value of extinction versus relative humidity based on MABL aircraft measurements from Durkee (1984). The functional relationship between these variables (Eq. 2.9) is also plotted	25
2.7	Total atmospheric water vapor (kg/m^2) as a function of brightness temperature difference (K) from Dalu (1986)	29
2.8	Difference between ship measured and calculated water vapor as a function of relative humidity deviation from 80% from Dalu (1986)	30
2.9	Simplified depiction of humidity mixing ratio Q/ρ and potential temperature θ within the MABL	32
2.10	Saturation vapor density ($\text{g}/\text{cm}^3 \cdot 10^6$) as a function of temperature based on Bolton (1980)	33
2.11	An example of a temperature and relative humidity profile for a typical subsidence inversion. Modified from Nieman (1977)	35
2.12	Frequency of atmospheric ducting associated with subsidence inversions from Ortenburger (1978)	36
3.1	Model relative humidity profile with $\text{RH}(0) = 70\%$ and $\Delta z = 1000\text{m}$	40
3.2	Extinction corresponding to the relative humidity profile in Fig. 3.1	41
3.3	Model generated vapor density profile	42
3.4	Variable C as a function of varying MABL depth	46

4.1	Model and technique produced MABL depth and relative humidities. Model depth = 500 m	50
4.2	Model and technique produced MABL depths and relative humidities. Model depth = 1000m	51
4.3	Model and technique produced MABL depths and relative humidities. Model depth = 1500m	52
4.4	Model and technique produced MABL depths and humidities. Model surface humidity = 62%	53
4.5	Model and technique produced MABL depths and humidities. Model surface humidity = 78%	54
4.6	Vapor density for RH(0) = 62% (solid) and RH(0) = 78% (dotted compared to the saturation vapor density profile based on $T_{sfc} = 25$ $^{\circ}C$	57
5.1	Effect of input errors on technique MABL depth	65

ACKNOWLEDGEMENTS

I would like to thank the number of people who encouraged me by their interest in this project, and their positive remarks. Dr. Jim Boyle was exceedingly helpful with his invaluable assistance in debugging computer codes and his technical advice on numerical methods. Dr. Carlyle Wash carefully reviewed this thesis, and offered constructive technical and literary criticism. I am most indebted to Dr. Philip Durkee for his constant encouragement and direction. This project could not have been accomplished without his assistance. Finally, I would like to acknowledge my wife, Debbie. I offer her my heartfelt gratitude for her constant support, especially during the final few months of this undertaking.

I. INTRODUCTION

The applications of meteorological satellites have expanded dramatically in the last two decades. Starting with simple visible imagery, the list of satellite techniques now includes soundings, cloud-drift winds and inferred measurements of atmospheric constituents. Recently, many of these techniques have become multispectral in nature. These techniques can be combined to provide a second-order technique to accomplish a specific objective. In this study, techniques for estimating aerosol optical depth, total atmospheric water vapor and sea-surface temperature are combined to yield a new technique for estimating marine boundary layer structure.

Currently, the marine boundary layer is primarily observed through conventional methods. These data originate from shipboard, island and coastal rawinsonde launches and near surface weather observations. In recent years, ground-based sodar (Gaynor and Mandics, 1978) and lidar (Eloranta *et al.*, 1975) have been used to remotely observe the boundary layer. These observations are spatially limited and rely on a dense network of measurement sites to provide a complete view of boundary layer variation in space and time. Development of reliable boundary layer characterization using satellite methods would expand the measurement area and eliminate the logistical concerns of maintaining a data gathering network.

The marine boundary layer is well-marked beneath strong subsidence inversions over subtropical oceans. The layer consists of a thin near-surface layer, a well-mixed layer and the capping subsidence inversion. Boundary layer depth is controlled by a balance between free atmosphere subsidence, surface fluxes of heat and moisture, and entrainment through the inversion. The degree of boundary layer instability influences the amount of turbulence available for mixing. Therefore, the degree of vertical homogeneity within boundary layers may vary.

Direct boundary layer measurements using satellite sounding are considered difficult at best. The spectral weighting functions for temperature retrieval schemes (Smith and Woolf, 1978) lack required vertical resolution and tend to smooth out smaller scale structure. Chesters *et al.* (1983) conclude that water vapor sounding is more difficult than temperature sounding. Water vapor weighting functions have a broad vertical extent, the vapor is usually concentrated just above a relatively high

brightness temperature background and radiance contributions from atmosphere are a nonlinear combination of both air temperature and water vapor content.

Observations of the marine boundary layer indicate that both marine aerosol and moisture are chiefly confined below the marine boundary layer inversion. The technique presented in this study takes advantage of this using satellite estimates of optical depth and total water vapor. These parameters can be estimated on a pixel by pixel basis with NOAA's Advanced Very High Resolution Radiometer (AVHRR). It will be shown that these estimates of optical depth, water vapor and sea-surface temperature can be combined to gain information about boundary layer depth and relative humidity. The sea-surface temperature measurement is required to close the set of mathematical equations which comprise the technique.

The link between aerosol particle size variations within the marine boundary layer, and satellite measured upwelling radiance was demonstrated by Durkee *et al.* (1986). Since marine aerosol particles are generated by evaporating droplets from bursting seawater bubbles (Woodcock, 1953), they are composed of primarily water soluble material. Hanel (1976) demonstrated that water soluble particle size increases with increasing relative humidity, particularly at levels higher than about 70%. As particle size increases, extinction increases, implying that upwelling radiance should increase. Durkee *et al.* (1986) verified this hypothesis in a case study off coastal California.

Total water vapor content may be retrieved from radiometric measurements as shown by Prabhakara *et al.* (1979), and Prabhakara and Dalu (1980). Dalu (1986) presented a technique for measurement of total water vapor from AVHRR channels 4 and 5. This method takes advantage of differential water vapor absorption between the channels to estimate near surface water vapor.

This thesis will capitalize on these satellite estimates of optical depth and water vapor. The objectives of this thesis are twofold:

1. Show that the independent measurements of optical depth and total water vapor may be combined to yield boundary layer depth and relative humidity structure. This will be accomplished by expressing the equations for optical depth and water vapor in terms of relative humidity.
2. Develop a parameterization for the vertical relative humidity profile that allows for reasonable representations of extinction within the layer.

In Chapter II, the theoretical background behind the measurements of optical depth and total water vapor is presented in terms of the governing radiative transfer

equations. Marine boundary layer structure and dynamics are reviewed and pertinent assumptions are stated. The definitions of optical depth and water vapor are presented in terms of relative humidity. In Chapter III, the measurements of optical depth and water vapor are combined with the sea-surface temperature to yield boundary layer surface humidity and depth. The relative humidity profile parameterization is presented and the iterative nature of the technique is discussed. Chapter IV describes a simulated boundary layer, which was developed to test the technique's performance for various depths and surface humidities. Systematic tendencies of the technique are then identified. In Chapter V, the sensitivity of the technique to errors in the measured inputs is discussed. The link between these inputs and the technique estimation of the surface humidity is examined. The final chapter presents the conclusions drawn from this thesis as well as recommendations for future work.

II. THEORETICAL BACKGROUND

It is proposed that the height of the marine atmospheric boundary layer (MABL), and a parameterization of the relative humidity profile within the layer may be indirectly determined by satellite. The described technique requires that optical depth, total atmospheric water vapor and sea-surface temperature be extracted from multispectral satellite radiance measurements. The technique utilizes channels 1, 4 and 5 of the Advanced Very High Resolution Radiometer (AVHRR). In addition, an estimate of the sea-level pressure is required. In this chapter, basic radiative transfer governing the measurements of optical depth and water vapor are reviewed, the relationship between optical depth and water vapor within the well-mixed MABL is developed and assumptions of the technique are presented.

A. MEASUREMENT OF OPTICAL DEPTH

In this section, it will be shown that the amount of radiance reflected by the atmosphere measured at the satellite is directly proportional to the amount of optically active scatterers in the atmosphere (optical depth). The ability of aerosol to effectively contribute to scatter is dependent on the composition, number and, most importantly, size of the aerosol. Variations in aerosol characteristics within the MABL occur due to changes in the prevailing wind speed and variations in the relative humidity in the layer. It will be shown that within the MABL the dominant variable in effecting change in aerosol characteristics is relative humidity.

1. Radiative Transfer to Estimate Optical Depth

The general form of the radiative transfer equation governing the scattering of solar radiation in the atmosphere may be written, after Liou (1980), as:

$$\begin{aligned} \mu \frac{dL(\tau, \Omega)}{d\tau} = & L(\tau, \Omega) \\ & - \frac{\omega_0}{4\pi} \int_{4\pi} L(\tau, \Omega') P(\Omega, \Omega') d\Omega' \\ & - \frac{\omega_0}{4\pi} \pi F_0 P(\Omega, \Omega_0) \exp(-\tau/\mu) \end{aligned} \quad (2.1)$$

where:

- L = diffuse intensity or radiance,
- τ = optical depth,
- ω_0 = single scatter albedo,
- μ = $\cos \theta$ (θ is the observation zenith angle),
- Ω = solid angle (θ, φ) (φ = azimuth angle),
- $P(\Omega, \Omega')$ = scattering phase function in scattering from solid angle Ω' to Ω and
- πF_0 = incoming radiative flux.

The first term on the right side of the equation describes the intensity absorbed or scattered from the beam. The second term accounts for the intensity added to the beam by multiple scattering from all solid angle, Ω , while the third term is the contribution to the beam by singly scattered photons.

The single scattering approximation simplifies Eq. 2.1. For radiance scattered once by marine aerosol, the radiative transfer equation becomes:

$$L(\tau; \mu, \varphi) e^{-(\tau_1 - \tau) \mu} = \frac{\omega_0}{4\pi} \pi F_0 P(\mu, \varphi; -\mu_0, \varphi_0) \int_{\tau}^{\tau_1} \exp\{-[(\tau' - \tau) \mu + \tau' \mu_0]\} d\tau' \mu \quad (2.2)$$

where:

- τ = optical depth at any level,
- τ_1 = total optical depth for a finite atmosphere and
- μ_0 = $\cos \theta_0$ (θ_0 is the solar zenith angle).

The single scattering approximation considers incident solar radiance as the only intensity source, and the intensity field due to single scatter of the source is calculated.

Assuming that the upward intensities from the ocean surface and subsurface are negligible, the reflected intensity for a finite atmosphere with total optical depth (τ_1) is:

$$L(0; \mu, \varphi) = \frac{\omega_0 \mu_0 F_0}{4(\mu + \mu_0)} P(\Theta) \left\{ 1 - \exp\left[-\tau_1 \left(\frac{1}{\mu} + \frac{1}{\mu_0}\right)\right] \right\} \quad (2.3)$$

The single scattering approximation applies to atmospheres with small optical depths. If $\tau_1(1/\mu + 1/\mu_0) \ll 1$, Eq. 2.3 becomes:

$$L(0;\mu,\varphi) \sim \frac{\omega_0 F_0}{4\mu} P(\Theta)\tau_1 \quad (2.4)$$

This equation shows that reflected intensities are directly proportional to the single scattering albedo, the scattering phase function, the satellite viewing geometry and are a linear function of optical depth.

Optical depth is the integration of the extinction coefficient (β_{ext}) through the depth of the atmosphere (dz):

$$\tau = \int_0^{\Delta z} \beta_{\text{ext}} dz \quad (2.5)$$

The extinction coefficient is comprised of extinction due to scattering (β_{scat}), and to absorption (β_{abs}). The extinction coefficient, or extinction, has the units of length^{-1} , and, by convention, is expressed in dimensions of km^{-1} . Consequently, optical depth is a dimensionless quantity that describes the amount of attenuation within the atmosphere.

The single scattering albedo is defined as:

$$\omega_0 = \frac{\beta_{\text{scat}}}{\beta_{\text{ext}}} \quad (2.6)$$

This variable can take on values from 0 to 1. A non-absorbing, scattering medium would correspond to $\omega_0 = 1.0$, while a completely absorbing medium would have an $\omega_0 = 0.0$. Shettle and Fenn (1979) observed that ω_0 is approximately 1.0 for marine particles. Variations in ω_0 from 1.0 are important since it is a direct multiplier of optical depth in Eq. 2.4.

The scattering phase function, $P(\Theta)$, describes the angular distribution of radiance scattered by particles. $P(\Theta)$ for marine particles at 80% relative humidity

shows a strong forward peak, indicating that these particles scatter primarily in the forward direction. It will be shown that changes in the particle size alter $P(\Theta)$. Therefore, as particle size changes, variations in the observed radiance are possible from the changing scattering phase function.

Observed radiance is highly dependent on the earth-satellite-sun geometry. Koepke and Quenzel (1979) discuss the optimal viewing geometries for observing atmospheric turbidity or optical depth. The hatched areas of Fig. 2.1 show favorable angles for turbidity measurements at given solar zenith distances (θ_s) and azimuths (ϕ). A favorable area is defined as an area where radiance variations with aerosol type are smaller than $\pm 4\%$. Regions of sunglint and areas close to the horizon are not suitable for turbidity determination. The dotted areas of Fig. 2.1 indicate regions of maximum sunglint. Any application of the technique presented in this study must account for the effects of geometry shifts on the measurement of the reflected radiance.

2. Effect of Radiometric Quantities on Optical Depth

An understanding of the radiometric quantities which effect optical depth are critical to the determination of how changes in the physical characteristics of the boundary layer will impact optical depth measurements. Changes in particle composition, numbers and size affect optical depth.

The scattering and extinction coefficients are defined as:

$$\beta_{\text{scat}} = \int_0^{\infty} \pi r^2 Q_{\text{scat}}(m,r) \frac{dN(r)}{dr} dr \quad (2.7)$$

and

$$\beta_{\text{ext}} = \int_0^{\infty} \pi r^2 Q_{\text{ext}}(m,r) \frac{dN(r)}{dr} dr , \quad (2.8)$$

where, πr^2 is the cross sectional area of a given particle radius, Q_{scat} and Q_{ext} are scattering and extinction efficiencies respectively (dependent on the complex index of refraction (m) and the particle radius (r)), and $dN(r)/dr$ describes the distribution of particles by radius. The index of refraction contains a real part (k) and an imaginary part (v). The real part determines the reflection or scattering by a medium and the

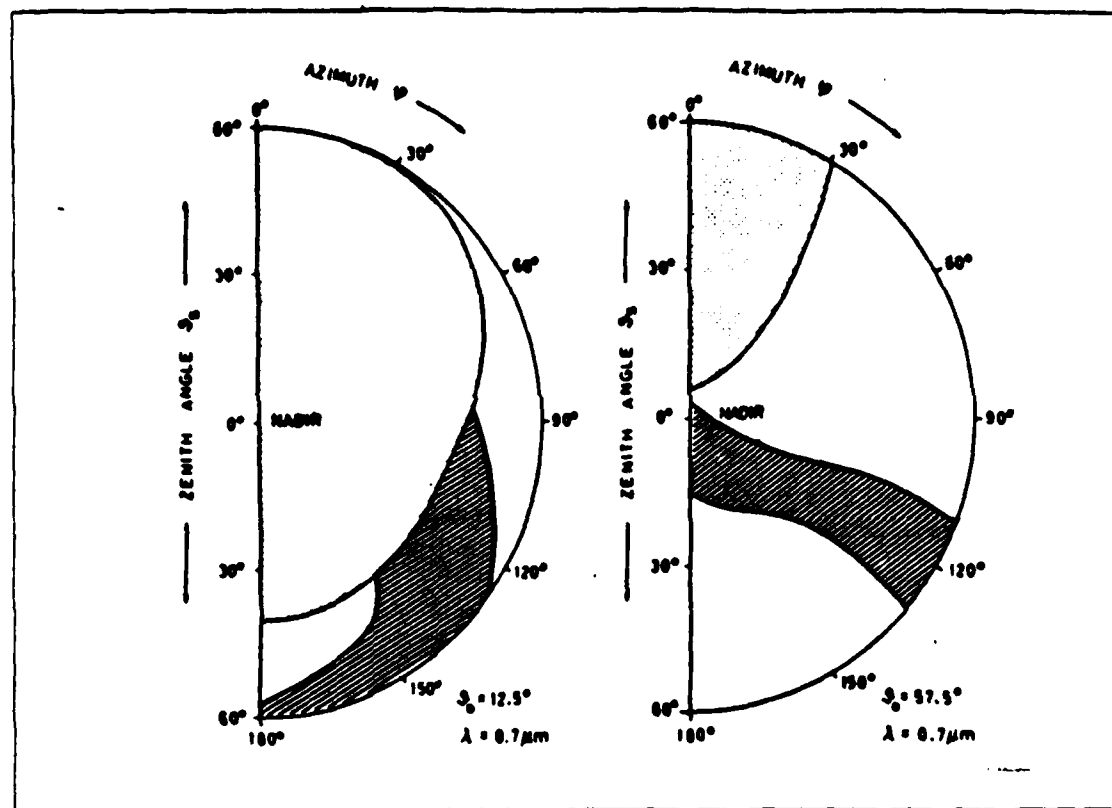


Fig. 2.1 Favorable viewing geometries for atmospheric turbidity with satellite zenith angles of 12.5° (left), and 57.5° (right). (Koepke and Quenzel, 1979).

imaginary part describes the amount of absorption by the medium at a given wavelength. Shettle and Fenn (1979) describe atmosphere aerosol distributions, and report k ranges from 1.33 for pure water to 1.53 for dust-like substances in visible and near-infrared wavelengths. For marine particles, v is less than 10^{-4} for wavelengths less than 1.0 microns. Therefore, absorption will be very small and the single scatter albedo ω_0 for marine particles is about 1.0. Since absorption is small, the scattering coefficient is very nearly equal to the extinction coefficient for marine particles. Thus, only extinction coefficient will be used in further discussions.

The extinction coefficient (Eq. 2.8) is the product of three factors summed over all particle radii. Variations in each of these factors result in changes in extinction. The three component terms of extinction as a function of radius for a relative humidity of 80% and a wavelength $\lambda = 0.694 \mu\text{m}$ are shown in Fig. 2.2 from Durkee (1984). The cross sectional areas and scattering efficiencies as a function of

particle size are shown in panels a and b respectively. Shettle and Fenn's model of marine particle size distribution at 80% relative humidity is depicted in panel c. The cumulative product of these three terms is shown in panel d. For smaller radii particles, i.e. $0.1\mu\text{m}$, the cross sectional area and extinction efficiencies are small, while the number of these small particles is large. Hence, the product of these terms leads to essentially no extinction. For larger particles, i.e. $10.0\mu\text{m}$, the cross sectional area is large, but the number of particles at this radius is small, so the effect on the cumulative extinction is slight. The portion of the cumulative extinction curve that has slope delineates those particle sizes which contribute most substantially to extinction. These particles range in size from 0.5 to $5.0\mu\text{m}$.

It can be seen from Eq. 2.8, that the characteristics of aerosol particles may change in three ways to alter extinction, optical depth and ultimately the radiance measured at the satellite. First, the composition of the particles can change, affecting the extinction efficiency through the index of refraction. Second, the total number of particles may change, influencing $N(r)$. Third, a change in particle size may change the size distribution $dN(r)/dr$.

a. Variations in Particle Composition

Particle composition changes are reflected in the index of refraction. For the range in the real part of the index, $k = 1.33$ to 1.53 , a small change in the reflected radiance occurs. Durkee (1984) showed that variations in upwelled radiance are negligible when compared to the sensitivity of channel 1 of the AVHRR sensor. Particle composition changes also alter the imaginary part of the index of refraction. The absorptive characteristics vary greatly for the different constituents of atmospheric aerosol. The range of v extends over several orders of magnitude from 0.5 for soot to 10^{-8} for pure water. Increasing the imaginary part of the index produces a reduction in ω_0 . Since ω_0 is a direct multiplier of Eq. 2.4, a similar reduction in upwelled radiance occurs.

b. Variations in Particle Numbers

Woodcock (1953) showed that aerosol particles within the MABL are primarily generated in the surface layer as wind-produced bubbles burst and droplets evaporate. Therefore, the total number of marine particles is wind speed dependent

Variations in the total number of particles with wind speed lead to variations in upwelled radiance through Eq. 2.8. Consequently, β_{ext} , τ and L are functions of the wind speed. Fig. 2.3 from Durkee (1984) shows the effect of changes

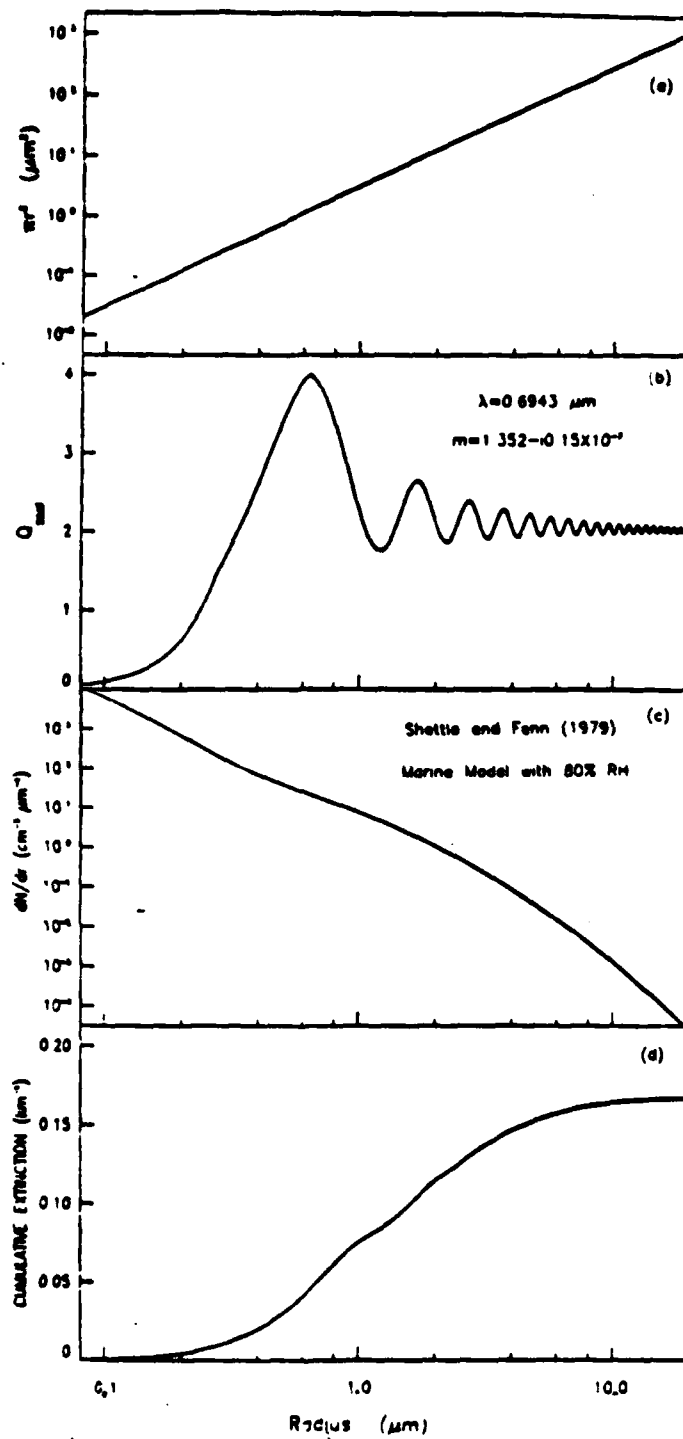


Fig. 2.2 The terms of the extinction formulation as a function of particle radius from Durkee (1984). See text for a more complete description of panels a,b,c and d..

in the prevailing wind speed on upwelled radiance based on particle number variations. The sensitivity of the AVHRR channel 1 sensor is shown. This figure shows that changes in the prevailing wind speed of 4 to 6 knots are sufficient to cause particle number variations of sufficient magnitude to produce detectable changes in upwelled radiance.

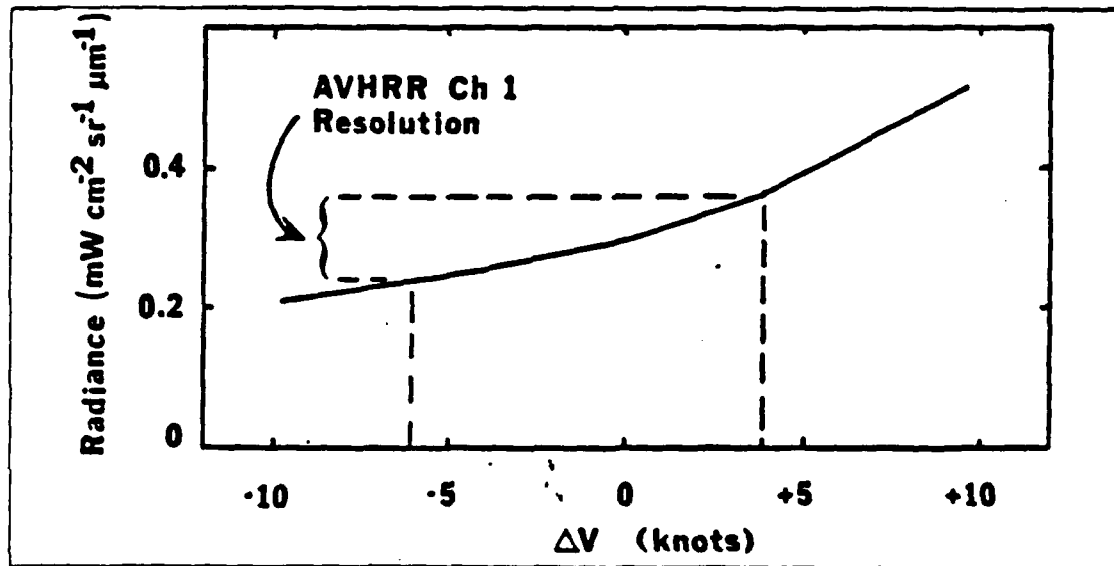


Fig. 2.3 Upwelling radiance variation for particle size variations as a result of wind speed variations. (Durkee, 1984).

c. Particle Size Changes with Relative Humidity

Hanel (1976) demonstrated that particle size changes significantly with relative humidity if the particles are composed of water soluble material. Since marine aerosol particles originate from evaporating sea-water droplets, the particle composition is mainly water soluble. Fitzgerald (1979) showed by theoretical and empirical data the relationship between particle size and relative humidity. For humidities in excess of 80%, particle size changes are strongly dependent on relative humidity variations. As relative humidity increases, particle size increases, enhancing the scattering ability of the particle population. This was verified by Fitzgerald *et al.* (1982) with nephelometer measurements.

As particles grow with increasing relative humidity, their composition consists of an increasing amount of liquid water. The real part of the index of refraction for sea salt and pure water is 1.49 and 1.33 respectively. The real part of the

index for these particles then decreases as relative humidity increases. As the scattering efficiency for the medium decreases, the corresponding upwelled radiance should undergo a similar reduction. However, it has already been shown above that any change in the real part of the index results in an undetectable change in AVHRR channel 1 sensor measurements of reflected radiance.

Changes in particle sizes due to changes in relative humidity also have an impact on the scattering phase function $P(\Theta)$. The effect of relative humidity changes on the phase function is illustrated in Fig. 2.4 from Durkee (1984). As relative humidity increases, the phase function becomes more forwardly peaked, while at side and back angles, the phase function value decreases slightly. As particle sizes decrease to the point of becoming much smaller relative to the wavelength of visible light, the scattering characteristics approach Rayleigh scattering behavior. The Rayleigh phase function is also plotted in Fig. 2.4.

The effects of increasing particle size and decreasing the refractive index with higher humidities is shown in Fig. 2.5. The sensitivities of channel 1 and 2 of the AVHRR sensor are also displayed. Durkee *et al.* (1986) concluded that radiance changes brought on by variations in relative humidity can be sufficiently large to be detected by the AVHRR instrument.

Table 1 indicates the extinction coefficients for various relative humidities at $0.694 \mu\text{m}$, corresponding to channel 1 of the AVHRR sensor. The table shows that an increase in relative humidity from 50% to 95% brings about an increase in the extinction coefficient of nearly an order of magnitude. For side and backscatter angles, with a similar increase in relative humidity, Fig. 2.4 shows the decrease in $P(\Theta)$ of less than a factor of 2. It can be concluded that even at angles where an increase in relative humidity causes a decrease in $P(\Theta)$, the effect of the increased extinction coefficient is dominant and higher relative humidity still results in increased upwelled radiances.

3. Optical Depth and Relative Humidity

Durkee (1984) used aircraft measurement of extinction within the MABL offshore southern California to find a relationship between extinction and relative humidity. The result was consistent with the Fitzgerald (1979) particle size-relative humidity relationship, and shows that changes in particle sizes are the overwhelming factor in producing variations in extinction. The data and curve fit to the observations are shown in Fig. 2.6. The measurements shown in Fig. 2.6 have been fit to a functional relationship between relative humidity and extinction:

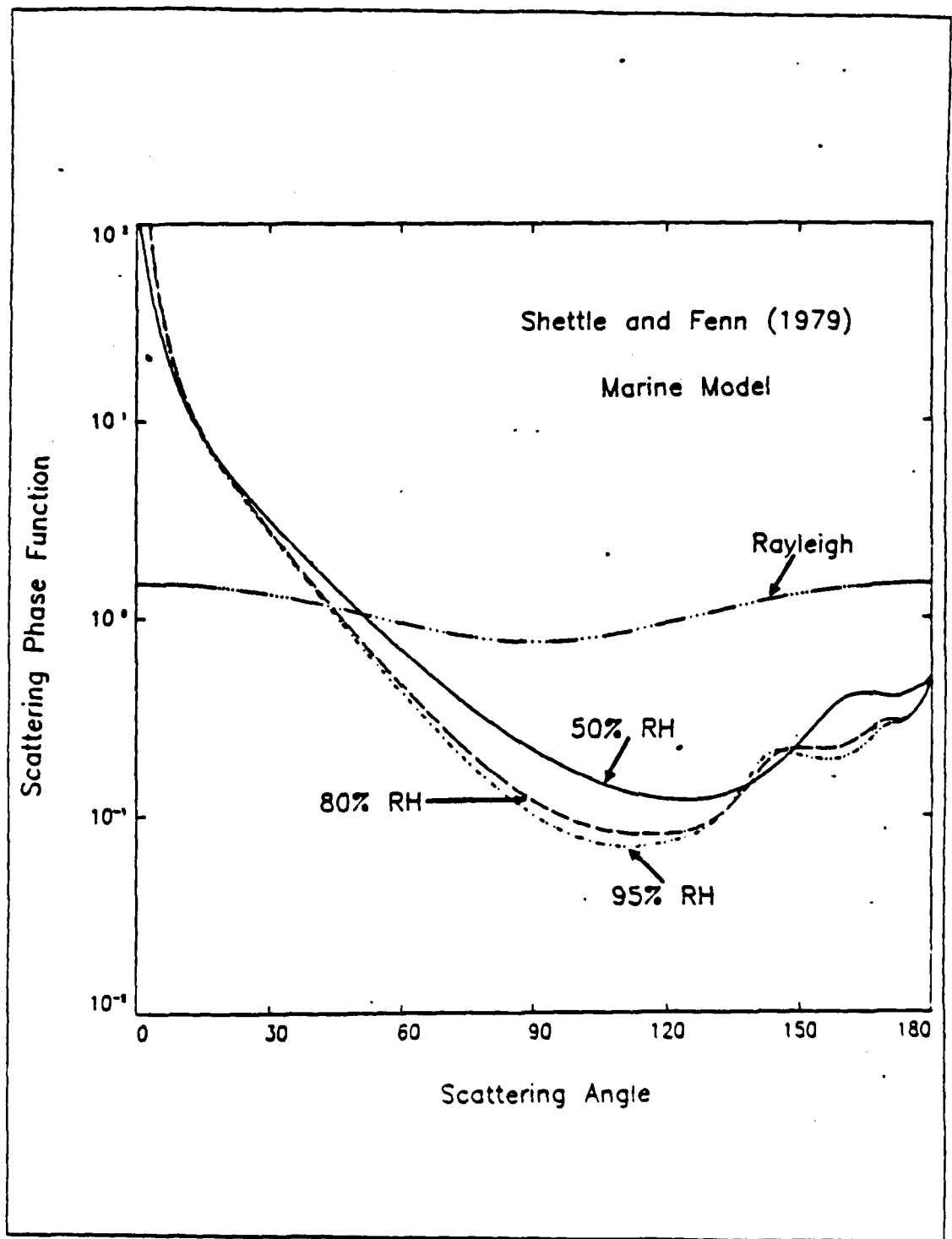


Fig. 2.4 Single-scattering phase function as a function of relative humidity. (Durkee, 1984).

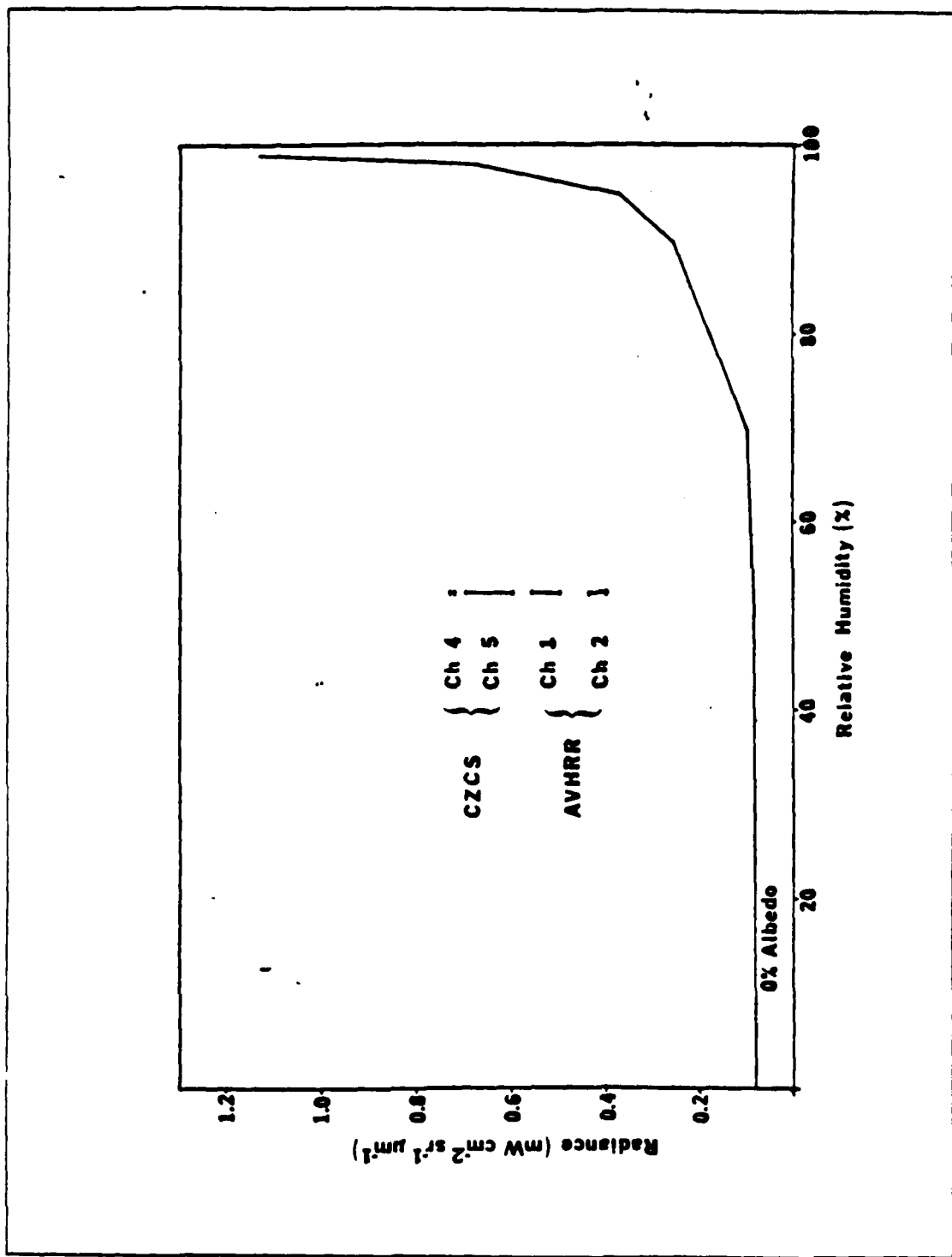


Fig. 2.5 Variation in upwelling radiance as a function of relative humidity from Durkee (1984).

TABLE 1
EXTINCTION COEFFICIENT VERSUS RELATIVE HUMIDITY

RH(%)	50	80	95
$\beta_{\text{scat}}(\text{km}^{-1})$	0.059	0.183	0.379

$$\beta = \frac{1}{A(B - RH)} \quad , \quad (2.9)$$

where, $A = .2998$ and $B = 99.8999$.

Using Eq. 2.5, optical depth may be solved for analytically when substituting Eq. 2.9 for extinction as a function of relative humidity:

$$\tau = - \frac{1}{A} [A(B - RH(z))] \Big|_0^{\Delta z} \quad , \quad (2.10)$$

where A and B are defined above, $RH(\Delta z)$ is the relative humidity at the top of the MABL, and $RH(0)$ is the surface relative humidity.

In summary, it has been shown that the optical depth is the vertical integral of the extinction coefficient. Under the assumption that the extinction is primarily resident only within the MABL, the only contribution to optical depth originates from this portion of the atmosphere. Variations in relative humidity will influence the magnitude of the extinction coefficient and optical depth through changes in particle size, and therefore directly effect the radiance measured by the AVHRR sensor.

B. MEASUREMENT OF WATER VAPOR

The second required quantity is water vapor near the earth's surface. The multispectral technique is related to a method described by Prabhakara *et al.* (1974) for the measurement of sea surface temperature. Prabhakara's method extracts sea-surface temperature from water vapor contaminated brightness temperatures by eliminating errors due to differential water vapor absorption across the 10 to 13 μm spectral range. However, instead of correcting for water vapor absorption, as in the

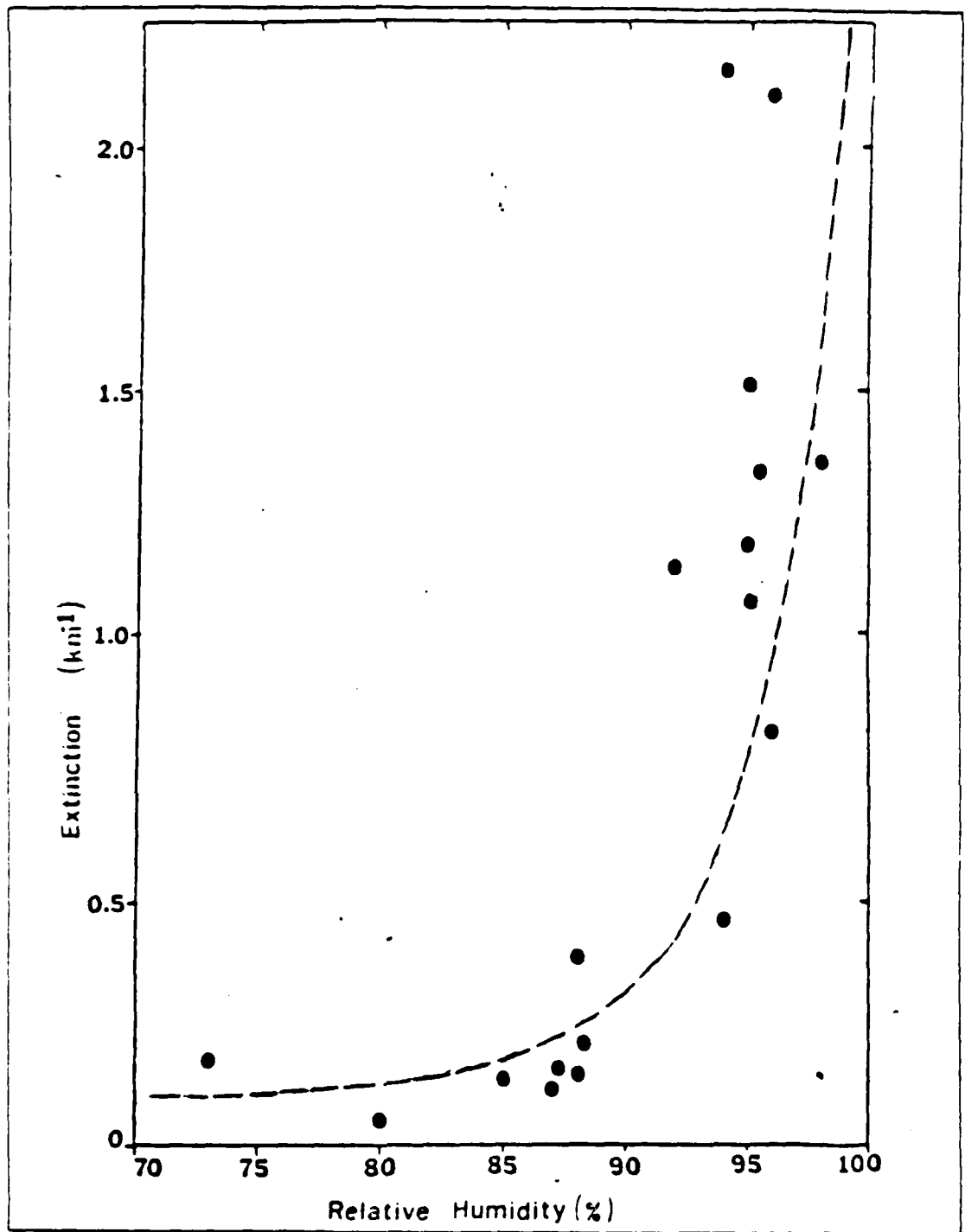


Fig. 2.6 Value of extinction versus relative humidity based on MABL aircraft measurements from Durkee (1984). The functional relationship between these variables (Eq. 2.9) is also plotted.

sea-surface temperature measurement, the varying degrees of absorptance may be utilized to provide information about the amount of water vapor present in the MABL.

1. Radiative Transfer and Satellite Techniques to Recover Water Vapor

The form of the solution of the radiative transfer equation governing a non-scattering, absorbing medium is Schwarzschild's equation. The generalized form presented by Liou (1980) for radiative transfer over a distance ds , from $s = 0$ to $s = s_1$, is given by:

$$L_{s_1}(\lambda)e^{-\tau(\lambda,1,0)} = \int_0^1 B[\lambda, T_b(s)]e^{-\tau(\lambda,1,s)} k(\lambda)\rho ds \quad (2.11)$$

where:

- L_{s_1} = radiance measured at $s = s_1$,
- L_0 = radiance emitted from $s = 0$,
- $B(\lambda, T_b(s))$ = blackbody emission from s and
- $k(\lambda)\rho ds$ = optical depth between points s and s_1 .

Applied to the atmosphere, the radiance measured by a remote sensor is equal to the emission from the earth's surface times the transmittance through the earth's atmosphere, plus the emission along the pathway from the earth's surface to the receiver times the transmittance from the level of emission to the receiver. For the 10 to 13 μm spectral range, Prabhakara *et al.* (1974) showed that Schwarzschild's equation may be approximated in terms of brightness temperature as:

$$T_B(\lambda, \theta) = T_s t_0(\lambda, \theta) + \bar{T}(\lambda)[1 - t_0(\lambda, \theta)] \quad (2.12)$$

where

- $T_b(\lambda, \theta)$ = brightness temperature at top of atmosphere,
- T_s = sea-surface temperature,
- t_0 = total transmittance of the atmosphere and
- $\bar{T}(\lambda)$ = mean radiative temperature of atmosphere.

Prabhakara *et al.* (1974) approximated Eq. 2.12 for the most transparent channel in the 10 - 13 μm band as:

$$T_s - T_1 \sim (T_s - \bar{T}_1)kW\sec\theta . \quad (2.13)$$

Here, k is equivalent to an absorption coefficient.

A nonlinear algorithm based on two observing channels within the 10 to 13 μm window was presented by Dalu *et al.* (1981) as a correction for atmospheric absorption to derive sea-surface temperature:

$$T_s - T_1 = g(W)(T_1 - T_2) , \quad (2.14)$$

where T_1 is the brightness temperature of the most transparent channel, T_2 is the brightness temperature of a second channel and $g(W)$ is a function of total water vapor. The function is described by :

$$g(W) = \frac{1 - t_1}{C(1-t_2) - (1-t_1)} . \quad (2.26)$$

The variables t_1 and t_2 are the transmittances of channels 1 and 2, and the coefficient $C = (T_s - \bar{T}_2)(T_s - \bar{T}_1)$ is a constant.

The combinations of Eqs. 2.13 and 2.14 through the term $(T_s - T_1)$ leads to an expression for total water vapor (W) in terms of the brightness temperature difference of the two channels:

$$T_1 - T_2 \sim \frac{k(T_s - T_1)}{g(W)}W\sec\theta . \quad (2.17)$$

Prabhakara *et al.* (1979) verified through a radiative transfer model that the ratio $(T_s - T_1)/g(W)$ remains approximately constant over a typical range of atmospheric water vapor contents.

The total water vapor content (W) in a column of atmosphere is defined as the vertical summation of the vapor density, ρ_w , within the column. Under the assumption that the total atmospheric water vapor is confined within the MABL, the vapor density must also reside in the MABL, and the integration distance (Δz) becomes the depth of the MABL:

$$W = \int_0^{\Delta z} \rho_w(z) dz \quad (2.16)$$

For AVHRR channels 4 and 5, 4 being most transparent, McMillin and Crosby (1984) found the atmospheric absorption correction ($T_s - T_4$) to be a linear function of the brightness temperature difference ($T_4 - T_5$):

$$T_s - T_4 = a(T_4 - T_5) + b \quad (2.18)$$

Eq. 2.18 may be further simplified for these channels as:

$$W = A(T_4 - T_5)\cos\theta \quad (2.19)$$

where $A = g(W)/(k(T_s - \bar{T}))$ remains nearly constant for typical atmospheric water vapor contents.

Dalu (1986) depicts water vapor content versus brightness temperature differences in Fig. 2.7. The slope of the line defines A to be $19.6 \text{ kg}/(\text{K}\cdot\text{m}^2)$. The data for Fig. 2.7 were obtained by applying Dalu's technique to a radiative transfer model to a wide range of atmospheric profiles of temperature and relative humidity. Surface relative humidity for these profiles was held constant at 80%. The correlation coefficient for the regression line is $R = 0.99$ and the error is given as $\pm 0.15 \text{ g}\cdot\text{cm}^2$.

A simulation of AVHRR channel 4 and 5 brightness temperatures for satellite water vapor retrievals was compared with ship measured data by Dalu (1986). An error increase to $\pm 0.5 \text{ g}/\text{cm}^2$ was observed. The added inaccuracy is due to the inexact spatial and temporal correlation of the satellite and ship measurements and the variation in the actual surface relative humidity from the control value of 80%. The error from the lack of spatial/temporal coincidence is not a factor for technique application, since ground-truthing of the measurement is unnecessary.

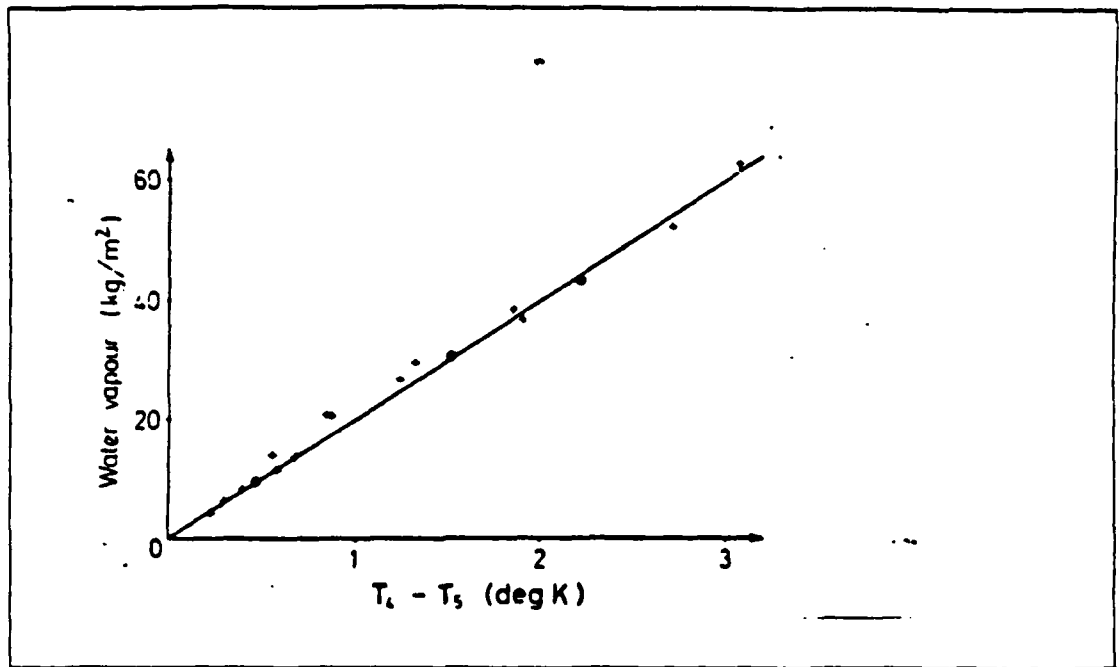


Fig. 2.7 Total atmospheric water vapor (kg/m^2) as a function of brightness temperature difference (K) from Dalu (1986).

Dalu (1986) points out that errors in retrieved water vapor may also be minimized by knowledge of the surface relative humidity. A comparison of data from ship measured and calculated water vapor in which the surface relative humidity varied from 80% suggests that improvements to the calculated results may be possible if the near surface relative humidity is known. Fig. 2.8 shows the possible correction that may be applied, in the form of a regression line drawn to the data points. Knowledge of the near surface relative humidity would allow a correction to the measurement of water vapor. The non-requirement of coincident surface data, plus the surface relative humidity correction would allow the accuracy of the water vapor measurements to approach $\pm 0.15 \text{ g}/\text{cm}^2$.

2. Total Water Vapor and Relative Humidity

Relative humidity depends on the vapor density and saturation vapor density of the ambient air within the boundary layer:

$$\text{RH} = \frac{\rho_w}{\rho_{ws}} \cdot 100\% \quad (2.20)$$

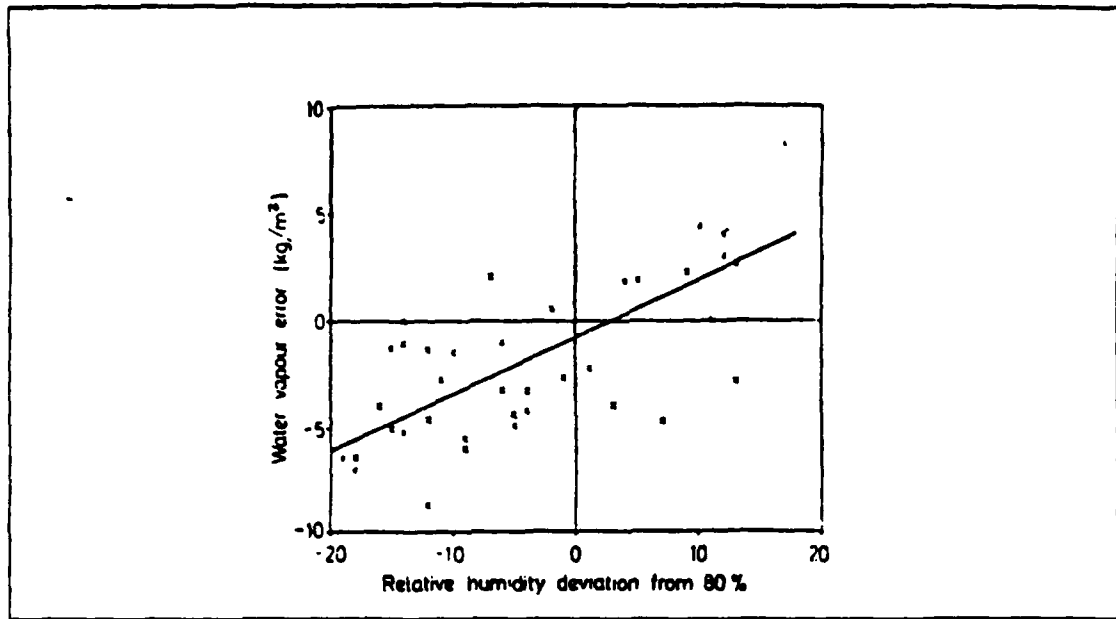


Fig. 2.8 Difference between ship measured and calculated water vapor as a function of relative humidity deviation from 80% from Dalu (1986).

Total atmospheric water vapor is the integral of the vapor density over the atmospheric column. Eq. 2.20 can be rewritten and substituted into Eq. 2.17 to obtain:

$$W = \int_0^{\Delta z} \frac{RH(z) * \rho_{ws}(T)}{100} dz . \quad (2.21)$$

If the integration extends through the depth of the MABL, consistent with the earlier assumption concerning W , and a constant mean layer vapor density is chosen, the integral can be solved such that:

$$W = \frac{RH(\Delta z/2) * \rho_{ws}(T(\Delta z/2))}{100} \Big|_0^{\Delta z} \quad (2.22)$$

C. MEASUREMENT OF SEA-SURFACE TEMPERATURE

Schwarzchild's equation (Eq. 2.11) also serves as the governing radiative transfer equation for sea-surface temperature measurement. Brightness temperatures measured at the satellite are generally lower than the actual sea-surface temperature because of water vapor absorption and reemission at lower atmospheric temperatures. Corrected sea-surface temperature measurements are accomplished by splitting the 10 - 13 μm window in order to take advantage of differential water vapor absorption across the window. The differential absorption is used to correct for water vapor attenuation. Currently, AVHRR channels 4 and 5 (channel 3 is also used at night) are utilized for measurement. The rms error from this method reported by McClain (1980) is less than 1.1°C.

D. CHARACTERISTICS OF THE MABL

The MABL exists, and varies in nature and depth, due to a balance of several processes. The controlling processes will be discussed, and the relationship between variables within the layer will be addressed.

1. Processes within the MABL

The classical MABL can be stratified into three horizontal layers (Fig. 2.9). The layer confined to the first 10 - 20 m above the sea surface is called the surface layer. Here, stability dependent fluxes of heat and moisture determine the vertical gradients of wind, temperature and moisture. The majority of the MABL, called the mixed layer, extends above the surface layer to the base of the subsidence inversion. This layer is dominated by turbulent eddies which mix temperature and moisture throughout the vertical extent of the layer. The relatively drier and warmer free atmosphere is separated from the MABL by an inversion layer. The inversion layer is typically characterized by strong vertical gradients in potential temperature and mixing ratio.

Turbulent eddies within the MABL act to entrain the free atmosphere into the mixed layer, thereby weakening the inversion layer, and warming and drying the MABL. Subsidence of the free atmosphere continually acts to force the MABL inversion layer toward the sea surface, strengthening the inversion layer. Herein, the basic descriptive balance of processes that govern the establishment and evolution of the MABL can be stated as:

1. Heat and moisture enter the base of the MABL through fluxes into the surface layer.

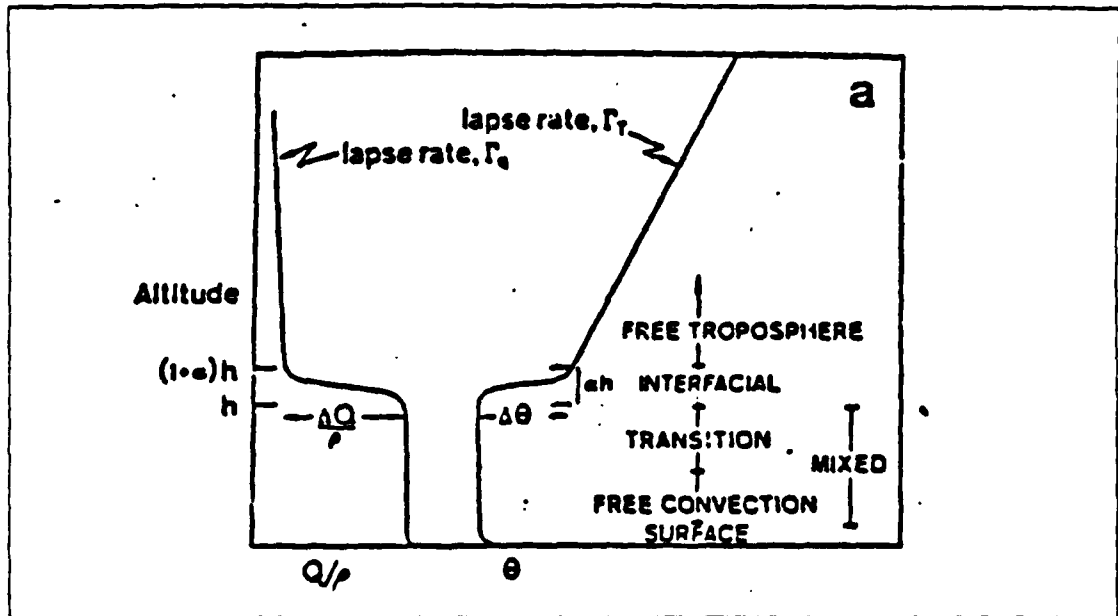


Fig. 2.9 Simplified depiction of humidity mixing ratio Q/p and potential temperature θ within the MABL.

2. Turbulent eddies in the mixed layer homogenize the layer, transport heat and moisture upward from the surface layer, and entrain free atmospheric air through the inversion layer.
3. Subsidence forces the MABL lower and intensifies the inversion layer.

2. Relationship Between Variables within the Well-Mixed MABL

The technique to be developed is based on relationships between temperature and relative humidity within the well-mixed MABL. The model MABL, developed to test the validity of the technique, was also constructed from these relationships. Observational data have substantiated these relationships in well-mixed layers.

Rogers (1979) presents a detailed discussion of the adiabatic mixing process, where samples of air from different pressure levels are brought adiabatically to the same pressure level and mixed. This is an ongoing process within the well-mixed layer of the MABL, where specific humidity, mixing ratio and vapor pressure tend to be constant with height. The potential temperature also becomes a constant value within a completely mixed layer and the temperature lapse rate approaches dry adiabatic.

Relative humidity depends on the vapor density and saturation vapor density of the ambient air within the boundary layer as shown in Eq. 2.20. The vapor density is a reflection of the amount of water vapor present within the air and is not

temperature dependent. Saturation vapor density has a direct temperature dependence. Bolton (1980) developed a formulation for saturation vapor density:

$$\rho_{ws} = \frac{6.11 \cdot 10^{\frac{7.5 \cdot T}{T + 237.3}}}{R_v \cdot (T + 273.16)} \cdot 10^{-4} \quad (2.23)$$

where temperature T is in $^{\circ}\text{C}$ and $R_v = .461 \text{ J/K-g}$. For $T > 0^{\circ}\text{C}$, this equation yields errors of less than 0.1%. Fig. 2.10 shows a plot of saturation vapor density as a function of temperature. Since the temperature lapse rate is dry adiabatic, relative humidity increases with decreasing pressure (increasing height) within the MABL.

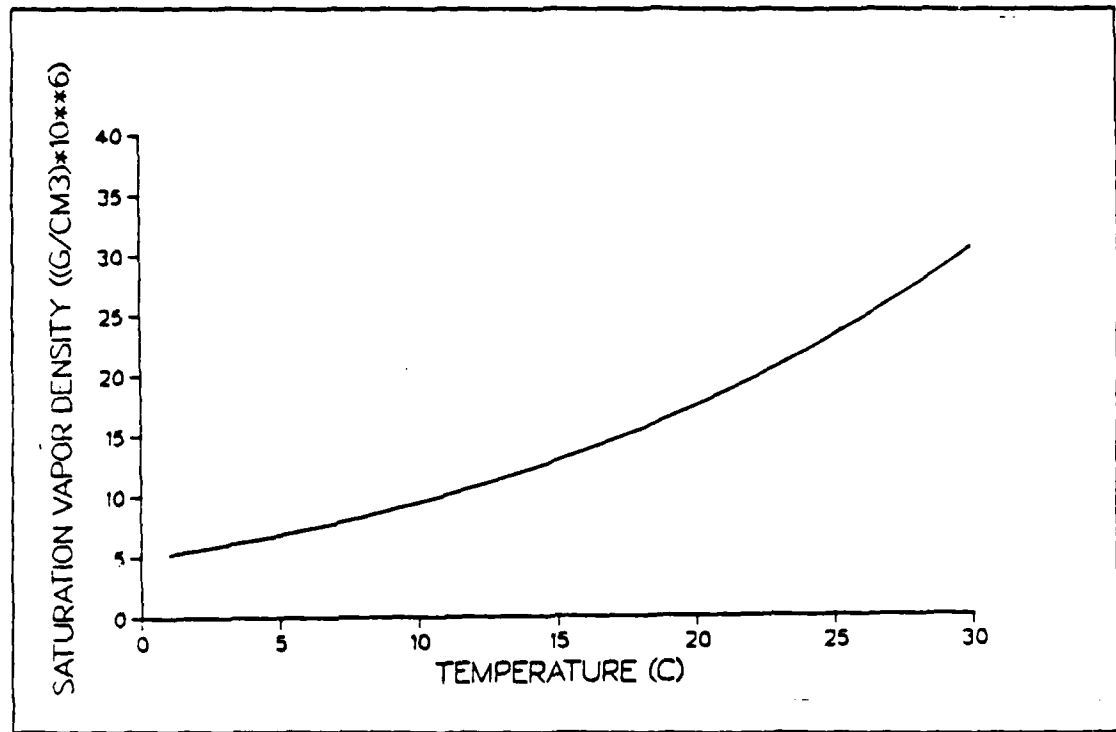


Fig. 2.10 Saturation vapor density ($\text{g}/\text{cm}^3 \cdot 10^6$) as a function of temperature based on Bolton (1980).

E. TECHNIQUE ASSUMPTIONS

The technique is based on three fundamental assumptions of the atmospheric structure:

1. Atmospheric optical depth at red-visible and near infrared wavelengths is confined primarily within the MABL.
2. The total atmospheric water vapor content is confined primarily within the MABL.
3. The MABL exists in an unsaturated, well-mixed state.

The validity of each of these assumptions requires some investigation to delineate conditions under which this technique may be properly applied.

1. Validity of Optical Depth within the MABL

Within this chapter, it has been shown that atmospheric optical depth is directly proportional to the amount of radiance reflected by the atmosphere. Scattering of solar radiation toward a satellite sensor results from several mechanisms. Rayleigh scattering occurs due to molecular constituents of the atmosphere. Away from strong gradients in temperature and pressure, Rayleigh scattering is nearly constant. Mie scattering results from atmospheric aerosol particles. In a cloud-free, marine environment, Mie scattering is primarily the result of marine particles within the MABL. Aerosols above the boundary layer, advected over water from continental sources, occasionally also contribute to Mie scattering. The distribution of continental aerosol, as shown by Pfeil (1986), is generally influenced by the circulation pattern of the atmosphere. Knowledge of continental aerosol production and transport then enables spatial prediction of relative concentrations. Finally, reflection of solar radiation from the ocean surface and from wind-induced whitecaps are a source of upwelled radiance. Koepke and Quenzel (1981) showed that ocean surface contributions to reflected solar radiance are minimized at red-visible and near infrared wavelengths which correspond to AVHRR channel 1.

2. Validity of Total Water Vapor within the MABL

Nieman (1977), and Agarwal and Ashajayanthi (1983) discuss maritime air masses associated with a strongly subsiding atmosphere. Within these air masses the subsiding motion of the mid-troposphere dries and warms the air mass. Over oceanic regions the lower troposphere is moistened by fluxes across the air-sea interface. The establishment of a moist MABL beneath a dry, free troposphere results. Fig. 2.11 shows a typical atmospheric sounding within this type of air mass. Under these regimes water vapor above the subsidence inversion is minimized and the assumption of total water vapor confined within the MABL becomes reasonable.

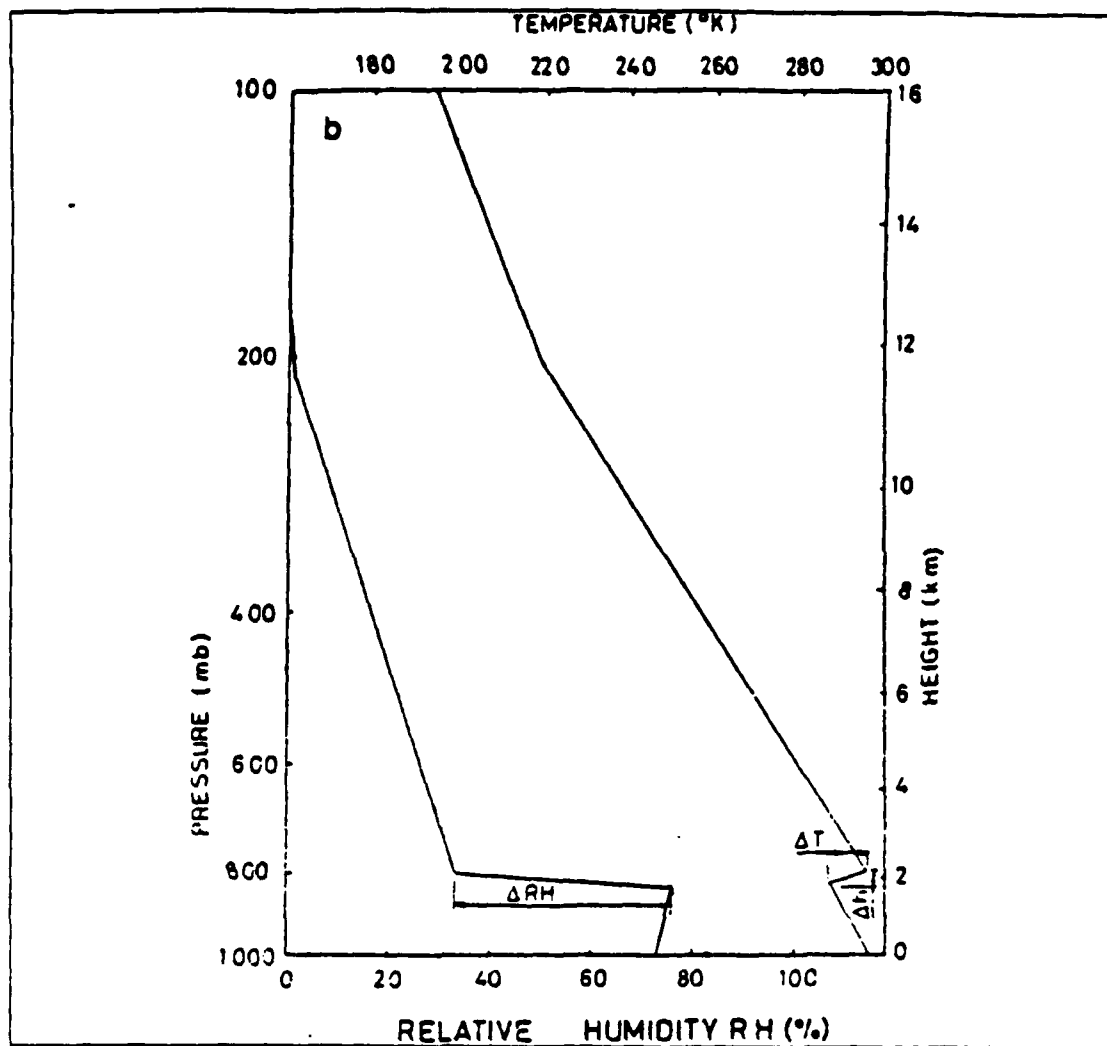


Fig. 2.11 An example of a temperature and relative humidity profile for a typical subsidence inversion. Modified from Nieman (1977).

Ortenburger (1978) shows regions of common occurrence of atmospheric ducting associated with subsidence-capped MABL's over oceanic regions in Fig. 2.12. These areas are geographically tied to the climatological locations of large subtropical anticyclones. The frequency of occurrence and subsidence inversion strength is increased in the summer hemisphere where the belt of subtropical anticyclones is stronger. Regions in which a relatively dry, free troposphere exists above the MABL may be inferred from the locations in which a high incidence of subsiding air masses occur. Occasionally, upper-level moisture from low latitude cut-off cyclones or jet

stream activity would increase the amount of water vapor in the upper troposphere. Detection of these features is possible from geostationary water vapor imagery.

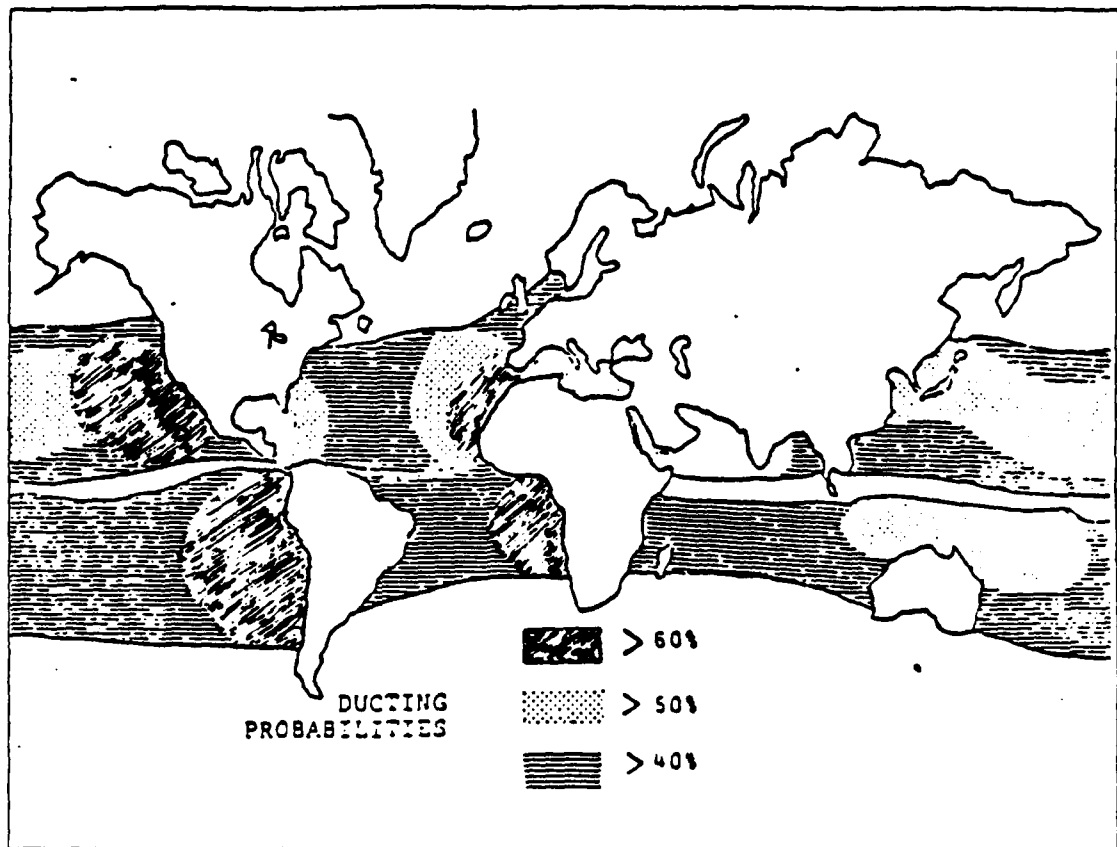


Fig. 2.12 Frequency of atmospheric ducting associated with subsidence inversions from Ortenburger (1978).

3. Validity of Well-Mixed MABL

The homogeneity of potential temperature and water vapor mixing ratio within the MABL is produced by turbulent mixing within the layer. Mixing eddies within the layer are a manifestation of buoyancy and shear effects. The formulation for buoyancy production, shown in Eq. 2.24, is stability dependent:

$$\pi_b = \frac{H g}{\rho c_p T} \quad (2.24)$$

where:

$H \rho c_p$ = specific temperature flux and
 $g: T$ = buoyancy factor.

The formulation for the shear production in Eq. 2.25 is dependent on the mean vertical wind speed gradient:

$$\pi_t = \frac{\tau du}{\rho dz} \quad (2.25)$$

where:

$\tau \rho$ = local momentum flux and
 $du dz$ = vertical wind shear.

The absence of strong buoyancy production within the subsidence produced MABL is due to the inability of the sea surface to warm significantly (in comparison to a land surface) during daylight hours. The lack of radiative cooling of the surface at night prevents the establishment of a stable layer. Thus, due to buoyancy effects alone, the MABL often remains nearly neutral with respect to stability with only slight diurnal variations.

The weakly unstable or neutral MABL is also influenced by wind shear. The effect of this shear is to increase the production of turbulent eddies which further mix the MABL. In most cases, the combination of buoyancy and shear produced turbulence can sufficiently mix the MABL.

In some regions of common subsidence inversions, the MABL is very stable, and mixing is suppressed. These regions would coincide with areas of relatively cold sea-surface temperatures, such as in coastal upwelling zones along the west coast of continents. In these regions, vertical distributions of the important state variables in the MABL deviate from those on which the technique was based. The response of the technique under these conditions still requires further investigation.

The assumptions required in this technique constrain its applicability. Satellite techniques for observing optical depth, total water vapor and sea-surface temperature require a cloud-free atmosphere. This technique has potential application in regions of subtropical anticyclones where water vapor above the MABL is minimized, away from continental aerosol above the boundary layer such that optical depth above the MABL is minimized and within well-mixed MABLs.

III. ESTIMATION OF MABL DEPTH AND RELATIVE HUMIDITY

This chapter details the technique of retrieving the MABL height and parameterized relative humidity profile. This technique is based on the theoretical background presented in the previous chapter. The solution is the result of an iterative process dependent upon optical depth, total water vapor, sea-surface temperature and estimated sea-level pressure.

The fundamental assumptions of optical depth and total water vapor confined within the MABL enable Eqs. 2.5 and 2.17 to be combined through the common vertical integration distance (Δz). It is first necessary to substitute for the extinction and vapor density in terms of relative humidity as a function of height. This will allow the combined equations to be solved for the surface relative humidity.

A. RELATIVE HUMIDITY PARAMETERIZATION

The selection of the following parameterization was based on relative humidity profiles inherent to the model atmosphere developed for technique validation. This model is consistent with the previously presented structure of the well-mixed MABL. The model will be presented in detail in the next chapter. Fig. 3.1 shows the model generated relative humidity profile for a 1000 m thick boundary layer. The profile can be seen to extend nearly linearly with height. As the layer becomes deeper, the simple linear parameterization becomes less valid. Linear versus model humidity profiles for various boundary layer depths will be compared in this chapter. The deviation from a linear profile may be explained using Eq. 2.20 and Fig. 2.10. In deeper layers the change in temperature through the depth of the layer is significant owing to the dry adiabatic lapse rate. This change in temperature allows the non-linearity of the saturation vapor density function, shown in Fig. 2.10 to influence the relative humidity profile through Eq. 2.20. As the boundary layer becomes thinner, the relative humidity profile can be approximated by a straight line. Therefore, the parameterization is a linear function of height:

$$RH(z) = RH(0) + Cz \quad , \quad (3.1)$$

where $RH(z)$ is the relative humidity at any height z , $RH(0)$ is the near-surface value and the factor C describes the change in relative humidity with height normalized to 1 km. The factor C was found in the model atmosphere to be variable with boundary layer depth. C will be discussed later in this chapter.

B. INTEGRATED OPTICAL DEPTH AND WATER VAPOR

The boundary layer optical depth was presented in Eq. 2.10. If extinction is again integrated with $RH(z)$ parameterized by Eq. 3.1, the result is:

$$\tau = -\frac{1}{AC} \ln \frac{AB - ARH(0) - AC\Delta z}{AB - ARH(0)} \quad (3.2)$$

As shown previously, extinction is highly non-linear with higher humidities. This makes it advantageous to seek an analytical solution (Eq. 3.2) for the integration of extinction, as opposed to a sum of layer averaged extinctions. Fig. 3.2 shows a plot of extinction versus height for the relative humidity profile presented in Fig. 3.1. Layer averaging of extinction would tend to underestimate the value of optical depth, particularly in deeper and moister MABLs.

Total water vapor was found by integrating a mid-layer value of vapor density under the assumption that the value at $\Delta z/2$ is representative for the MABL. Fig. 3.3 shows the model atmosphere vapor density profile for a 1000 m thick MABL. This figure shows MABL vapor density to be linear with height, allowing a mid-layer value to be representative of the entire layer. The formulation of the vapor density then, in terms of relative humidity and saturation vapor density (Eq. 2.20), must be accomplished with values of these variables at $\Delta z/2$. Total integrated water vapor can be then written as:

$$W = \frac{(RH(0) + C\Delta z/2)p_{ws}(T(\Delta z/2))}{100} * \Delta z \quad (3.3)$$

C. NEAR-SURFACE RELATIVE HUMIDITY AND MABL THICKNESS

Eq. 3.2 and 3.3 may be algebraically manipulated to solve for the layer depth (Δz):

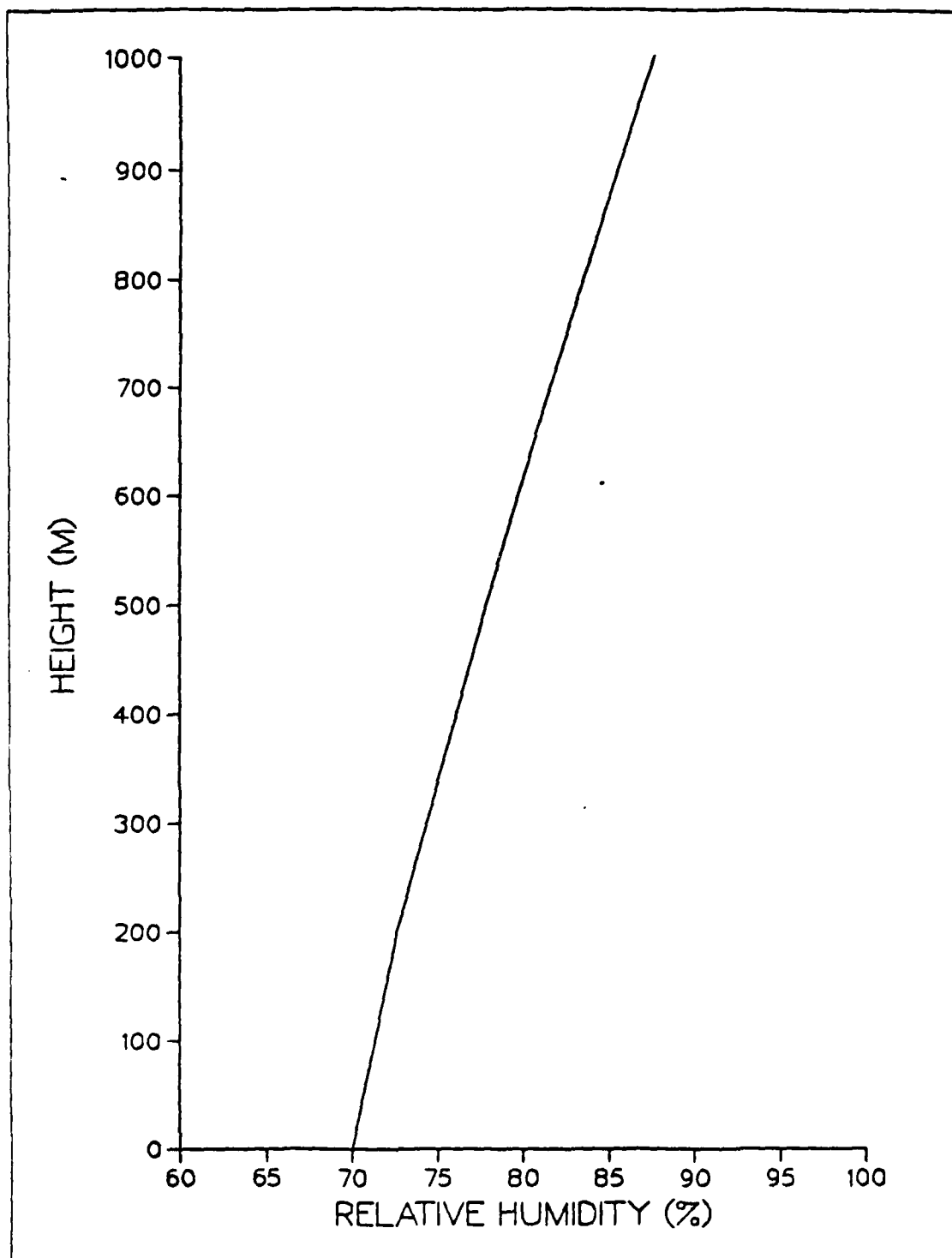


Fig. 3.1 Model relative humidity profile with $RH(0) = 70\%$
and $\Delta z = 1000m$.

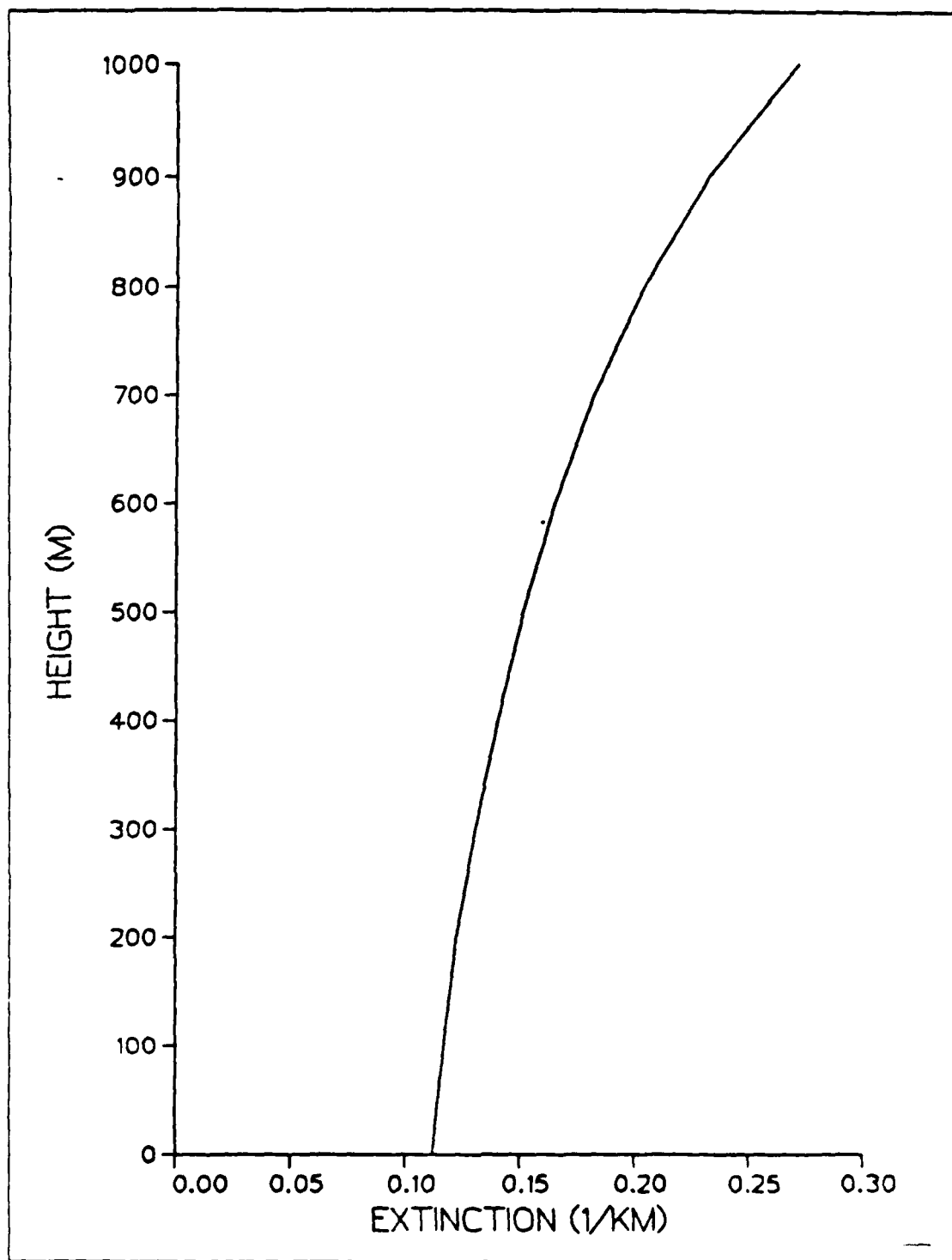


Fig. 3.2 Extinction corresponding to the relative humidity profile in Fig. 3.1.

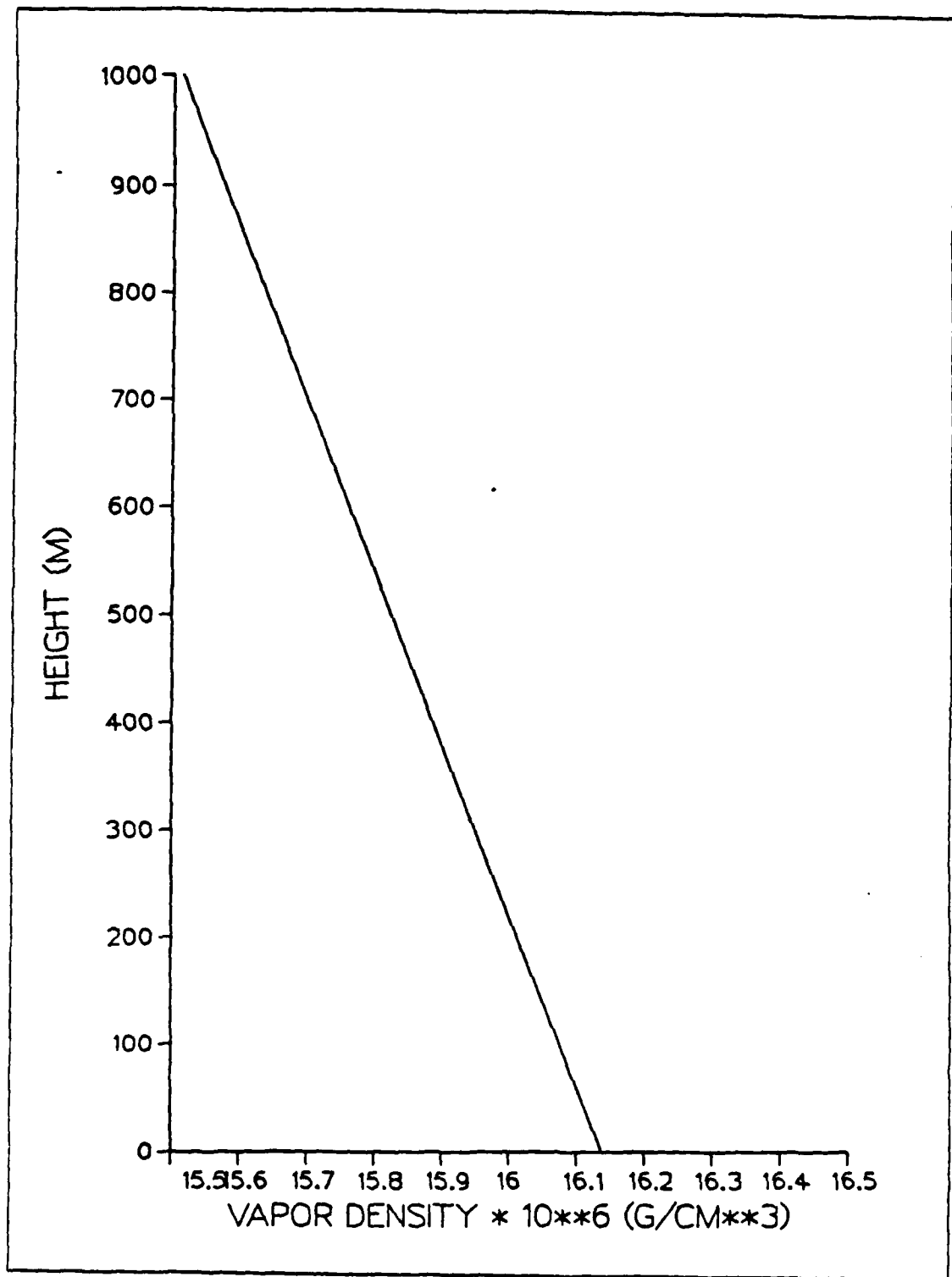


Fig. 3.3 Model generated vapor density profile.

$$\Delta z = \frac{AB - (AB - ARH(0))\exp(-\tau AC) - ARH(0)}{AC} \quad (3.4)$$

and

$$\Delta z = - \frac{RH(0) \pm \sqrt{RH(0)^2 + 200CW/\rho_{ws}(T_{lvr})}}{C} \quad (3.5)$$

In Eq. 3.5, the positive root of the radical is always selected to provide the meteorologically sensible solution. Eqs. 3.4 and 3.5 now may be combined through the common factor, Δz . Further manipulation leads to a quadratic equation in near-surface relative humidity, $RH(0)$:

$$\begin{aligned} & [1 - (e^{-\tau AC})^2] * RH(0)^2 \\ & + [2Be^{-\tau AC} (e^{-\tau AC} - 1)] * RH(0) \\ & - B^2(1 - e^{-\tau AC})^2 + 2.0 * 10^{-3} CW / \rho_{ws}(T_{lvr}) = 0 \end{aligned} \quad (3.6)$$

Solution of this quadratic formula gives the near-surface relative humidity value, and is then substituted into either Eq. 3.4 or 3.5 for determination of the MABL thickness.

The technique will fail if measurements of optical depth, total water vapor and sea-surface temperature are inconsistent. The failure occurs in solving the above quadratic equation for surface relative humidity, as the equation produces two complex numbers. If measurements are consistent, the complex numbers have imaginary parts equal to zero. Ambiguity does not exist between the two solutions since one is always obviously too low. If the input measurements are inconsistent, the imaginary portions of the complex numbers are non-zero and the surface relative humidity is indeterminate.

D. THE ITERATIVE PROCESS

The technique iterates on Eqs. 3.6 and 3.4, and converges to a near-surface relative humidity and boundary layer depth, provided that measurements of optical

depth, water vapor and sea-surface temperature are reasonably consistent. The layer saturation vapor density and the value of the variable C are redefined with every iteration of layer thickness. Iteration is necessary due to the initially limited information available about the MABL. Mid-layer temperature and layer thickness are unknown at the onset. After a calculation of the near-surface humidity is made, layer depth and mid-layer temperature can be determined. With these variables, redefined values of C and the layer saturation vapor density are determined. Since ρ_{ws} and C are factors in the quadratic equation for near-surface humidity, iteration is required.

1. Saturation Vapor Density

The initial value of the layer saturation vapor density is found from the sea-surface temperature. Successive iterated values are the mid-layer values as the hypsometric formula and Poisson's equation are applied to the computed layer thickness and temperature respectively. After the initial MABL height is found, the layer is subdivided into 4 equal sublayers (Δz_s), and the hypsometric formula is employed to determine the pressure at the top of the first sublayer:

$$P_{i+1} = P_i \exp \left(-g \Delta z_s / R \bar{T}_v \right) , \quad (3.7)$$

where P_i and P_{i+1} are pressures at the bottom and the top of the sublayer respectively, g is the acceleration of gravity and R is the universal gas constant. This step is initiated by an estimate of the surface pressure, the mean layer virtual temperature (\bar{T}_v) and knowledge of the sublayer thickness (Δz_s). Poisson's equation enables the computation of temperature at the top of the sublayer:

$$T_{i+1} = T_i (P_{i+1} / P_i)^{.286} . \quad (3.8)$$

A second use of the hypsometric formula and Poisson's equation for the second sublayer enables computation of the mid-layer temperature. This temperature is then the basis for the layer saturation vapor density.

The mean sublayer virtual temperature is not actually available due to the lack of moisture information required for its determination. A reasonable approximation may be found by using the temperature at the bottom of the sublayer. The error is minimized, since virtual temperature typically exceeds the ambient air temperature by a few degrees Centigrade due to atmospheric moisture, and the temperature at the

bottom of the sublayer exceeds the mid-layer temperature due to the adiabatic lapse rate.

2. C - Relative Humidity Variable

The variable C in Eq. 3.1 describes the percentage increase in relative humidity from the near-surface value, to the top of the layer when normalized to 1000 m. Computations of C were done for model boundary layers varying in depth from 300 to 1500 m. The plotted data and linear fit to the points is shown in Fig. 3.4. The equation of the plotted line was found to be:

$$C = 14.07 + 3.333(\Delta z) , \quad (3.9)$$

where Δz is the layer thickness in km and C is in dimensions of %/km. The initial value of this variable is chosen as 14.07 %/km with $\Delta z = 0$.

The technique is considered to have converged when the change in MABL depth between successive iterations reduces to less than 1 m. The speed of convergence is dependent on the relative depth of the MABL. For shallower layers near 500 m in depth, convergence occurs within 4 to 5 iterations. For boundary layer depths near 1500 m, convergence requires 5 to 7 iterations.

The converged values of near-surface relative humidity, MABL thickness and the variable C enable the parameterized relative humidity profile to be constructed. The relative humidity throughout the MABL is found through Eq. 3.1.

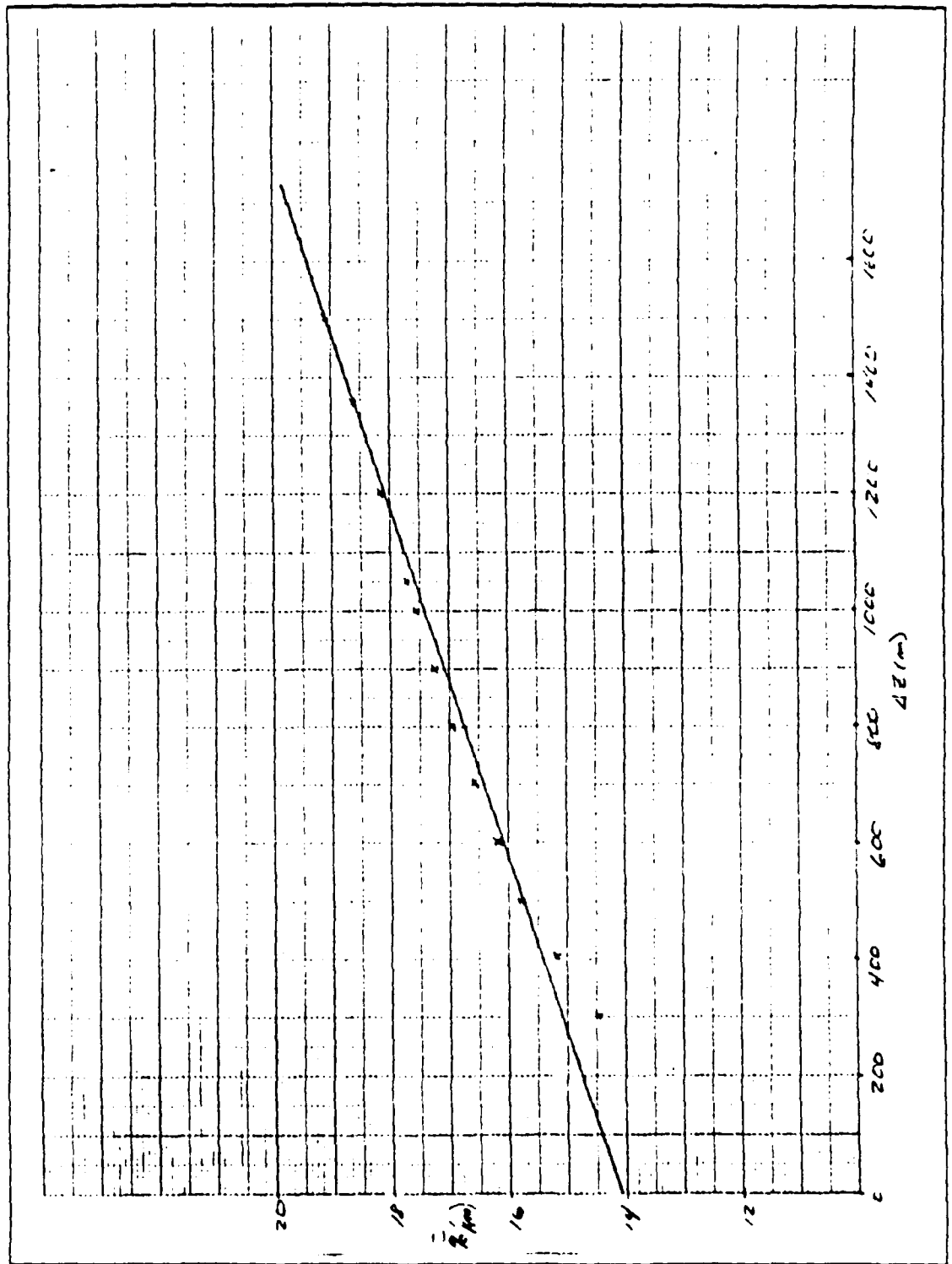


Fig. 3.4 Variable C as a function of varying MABL depth.

IV. TECHNIQUE RESPONSE TO A SIMULATED BOUNDARY LAYER

A simulated boundary layer was developed in order to test the accuracy of the technique in determining MABL depth and relative humidity structure. This layer was modeled after the well-mixed MABL described in Chapter II. The model was extended to three depths and ranged through three surface relative humidities in order to examine the technique's performance for a variety of MABL types.

A. MODEL STRUCTURE

This model is structured after the well-mixed portion of the MABL in which potential temperature and mixing ratio are conserved. Surface layer gradients of potential temperature and mixing ratio are not accounted for. The model extends upward to, but does not include, the subsidence inversion. The following is a description of how the model boundary layer was developed.

The model MABL is subdivided into 11 vertical levels, creating 10 equal depth layers of thickness $\Delta z/10$ m. Initially provided are the heights at the 11 levels, extending upward from the sea surface, the total layer thickness and surface values of pressure, temperature and relative humidity. The pressures and temperatures at each level are computed from the hypsometric formula and Poisson's equation in a fashion similar to that described in Chapter III to obtain a representative layer saturation vapor density. The use of Poisson's equation invokes the constant potential temperature assumption. The hypsometric formula initially estimates the mean MABL virtual temperature as the surface temperature minus 2°C. The first guess pressures and temperatures for each level are thereby determined. The densities of dry air, $\rho_d(i)$, for each level are computed from the equation of state for dry air:

$$\rho_d(i) = \frac{P(i)}{RT_k(i)}, \quad (4.1)$$

where $P(i)$ and $T_k(i)$ are pressures and absolute temperatures at level- i . Next, the assumption of constant mixing ratio is invoked to compute the level vapor densities, $\rho_w(i)$. Mixing ratio (w), defined as

$$w = \frac{\rho_w}{\rho_d} , \quad (4.2)$$

is known, based on the surface temperature, pressure and relative humidity. The vapor density at the adjoining upper level is:

$$\rho_w(i+1) = \rho_d(i+1) * \frac{\rho_w(i)}{\rho_d(i)} , \quad (4.3)$$

where variable subscripts i and $i+1$ refer to lower-and upper-level values respectively. Virtual temperature now can be computed for each level and averaged between levels to give layer values. Knowledge of the virtual temperature enables pressures, temperatures and densities of dry air and vapor to be recomputed.

Saturation vapor densities at each level are determined from the temperature profile through Eq. 2.23. Relative humidity is determined from Eq. 2.20 with vapor and saturation vapor densities. Layer values of each of these variables are found by averaging adjacent upper and lower level values. The layer averaged values of vapor density are vertically summed to give total water vapor (W).

Layer averaged values of relative humidity lead to layer extinctions through Eq. 2.9, which can be numerically integrated to give the boundary layer optical depth. However, the exact method of analytical integration of the extinction coefficient is used instead. This is preferable due to the strong nonlinearity of extinction with higher relative humidity.

The model atmosphere was developed with a surface temperature of 25°C and a surface pressure of 1025 mb. These values were chosen as being broadly representative of conditions under subtropical high pressure systems. A near-surface relative humidity of 70% was arbitrarily selected.

B. TECHNIQUE PERFORMANCE IN A SIMULATED MABL

The objective of applying the technique to a model boundary layer is to demonstrate the accuracy of the technique's estimates, and to observe possible systematic tendencies.

1. Variations in Layer Depths

'Shallow', 'intermediate' and 'deep' MABLs were modeled corresponding to depths of 500, 1000 and 1500 m. Figs. 4.1 to 4.3 depict both model and technique-estimated boundary layer depths and relative humidity profiles for the three MABL depths.

The technique estimate with the 500 m deep model MABL (Fig. 4.1) shows the surface relative humidity converged to a value of 69.83%, which is slightly below the model surface humidity of 70%. The final iterated value of layer thickness was 503 m, or slightly above the model MABL depth. Solution convergence occurred with 4 iterations.

The technique solution with a 1000 m thick MABL (Fig. 4.2) converged to a surface humidity of 70.24%, slightly exceeding the model value. The resulting layer thickness of 995 m was shallower than the model MABL depth. Convergence occurred in 5 iterations.

The estimated MABL structure is compared with the actual 1500 m deep MABL in Fig. 4.3. Surface relative humidity converged to 70.74% and the depth converged to 1470 m. Technique behavior was similar to that of the 1000 m deep MABL case in that the technique overestimated the surface relative humidity while it underestimated the layer depth. Convergence occurred in 7 iterations.

2. Variations in Surface Relative Humidity

Surface relative humidities of 62%, 70% and 78% for a 1000 m deep layer were also tested. The technique results, with the model depth and humidity profiles are shown in Figs. 4.4, 4.2 and 4.5.

The $RH(0) = 62\%$ case (Fig. 4.4) converged to a higher surface humidity, 63.44%, resulting in higher humidities throughout the depth of the MABL. Consequently, estimated layer depth was shallower than the model.

The 70% case is also the second case in the layer depth discussed above (Fig. 4.2). The converged surface humidity value of 70.24%, and the associated profile are nearly identical to the model structure as previously discussed.

In the $RH(0) = 78\%$ case (Fig. 4.5), the technique converged to a lower surface humidity, 77.65%, and hence the humidity values in the profile were less than those for the model profile. The departure increases with height due to the curvature in the model relative humidity profile. As anticipated, the resulting final MABL depth exceeded the model depth.

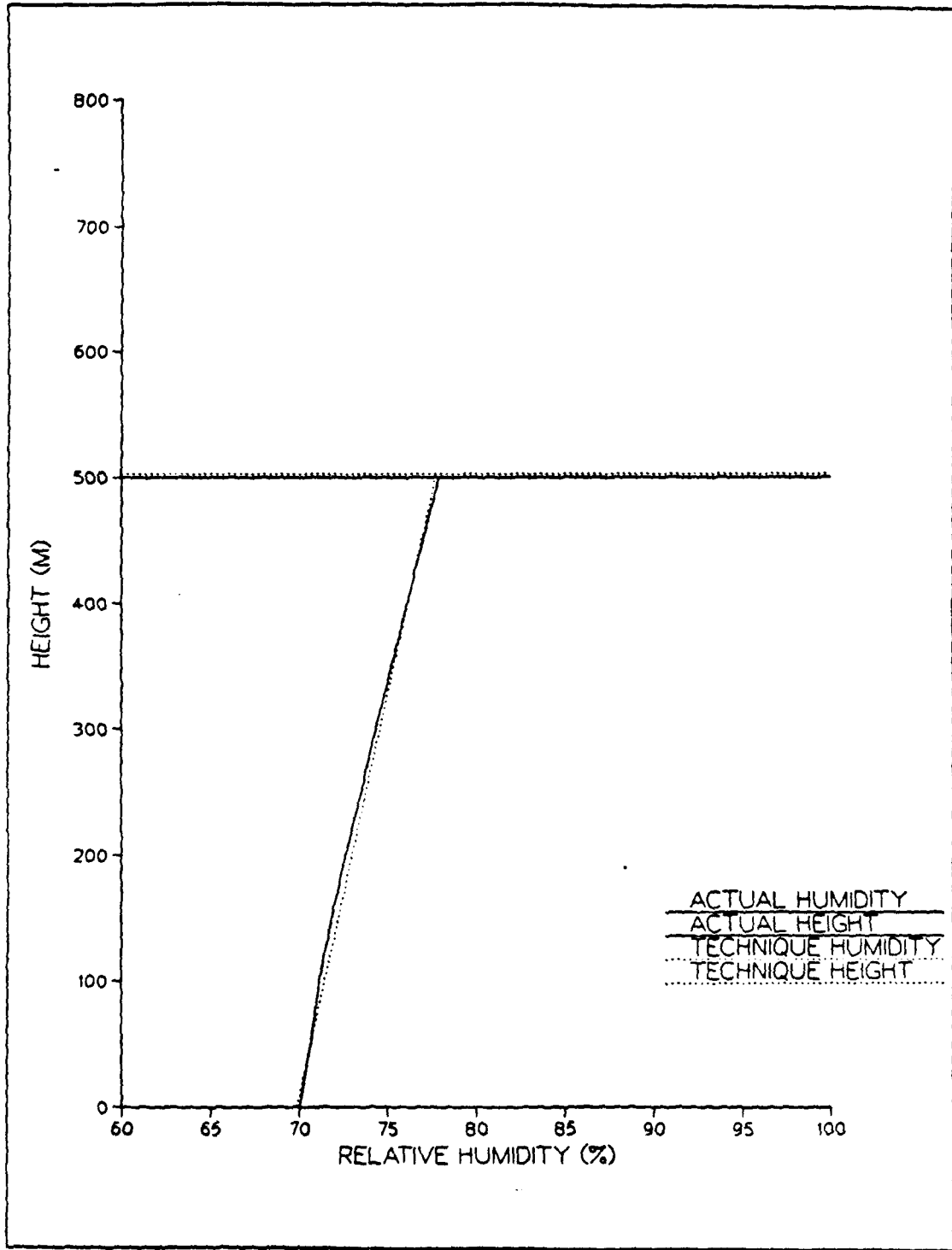


Fig. 4.1 Model and technique produced MABL depth and relative humidities. Model depth = 500 m.

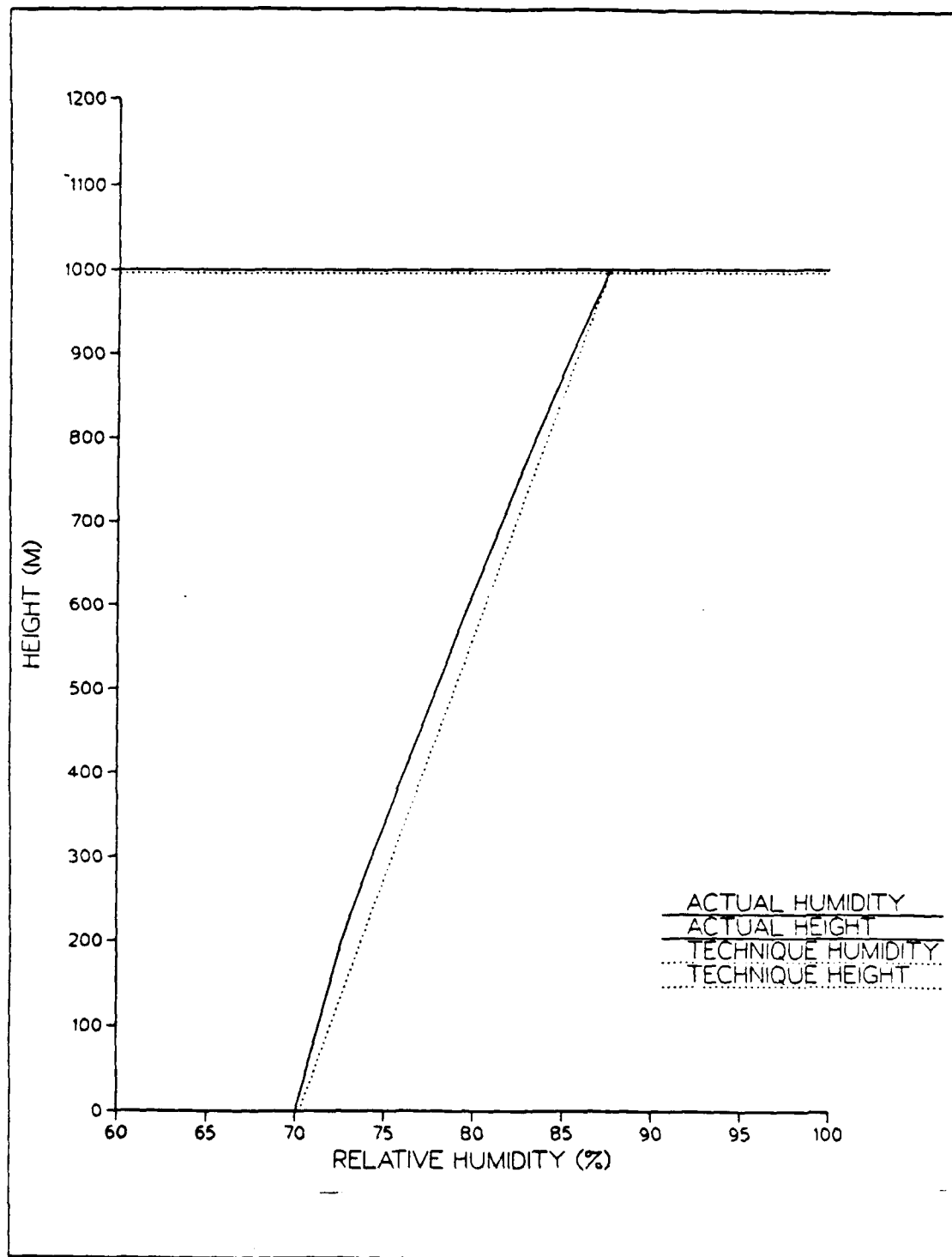


Fig. 4.2 Model and technique produced MABL depths and relative humidities. Model depth = 1000m.

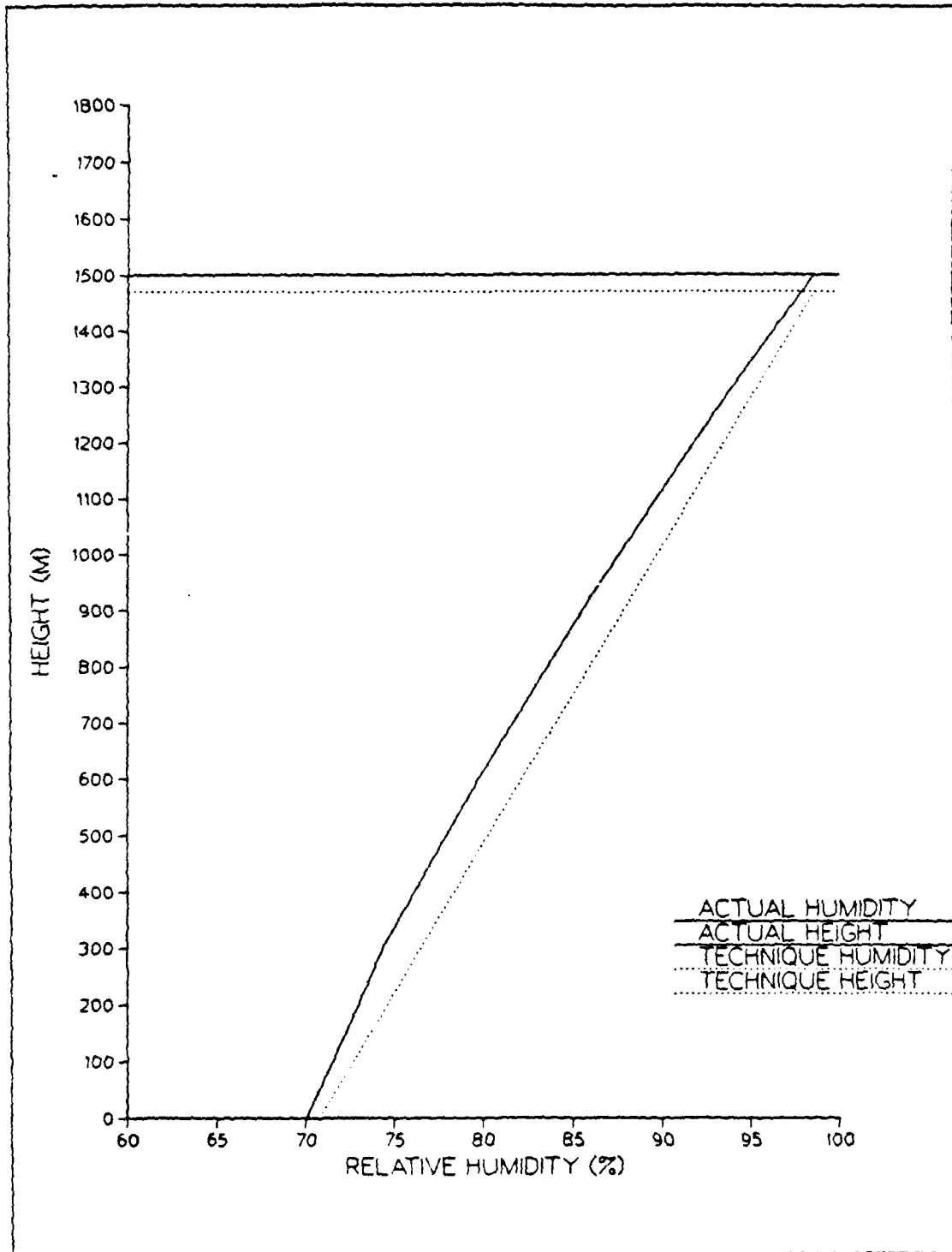


Fig. 4.3 Model and technique produced MABL depths and relative humidities. Model depth = 1500m.

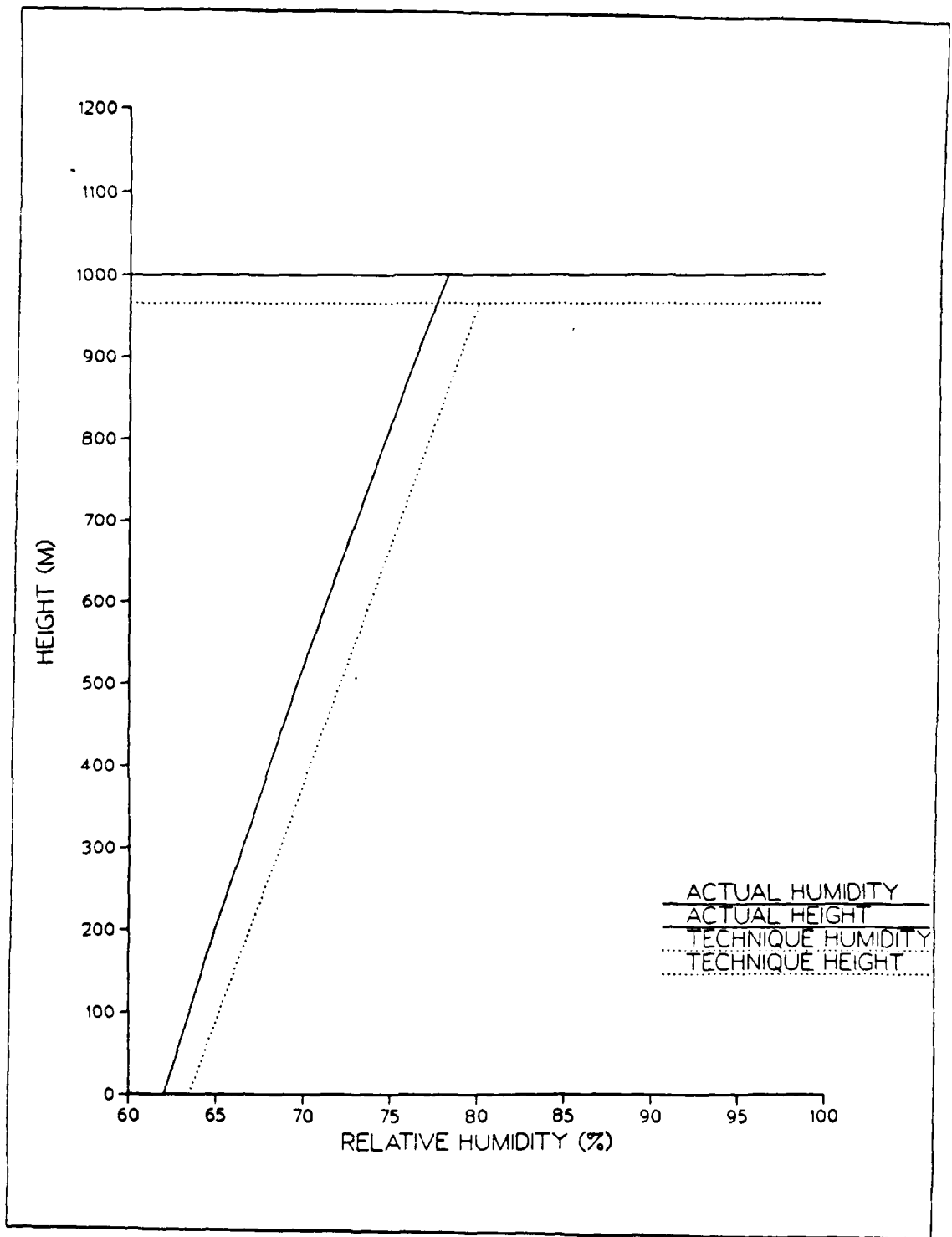


Fig. 4.4 Model and technique produced MABL depths and humidities.
 Model surface humidity = 62%.

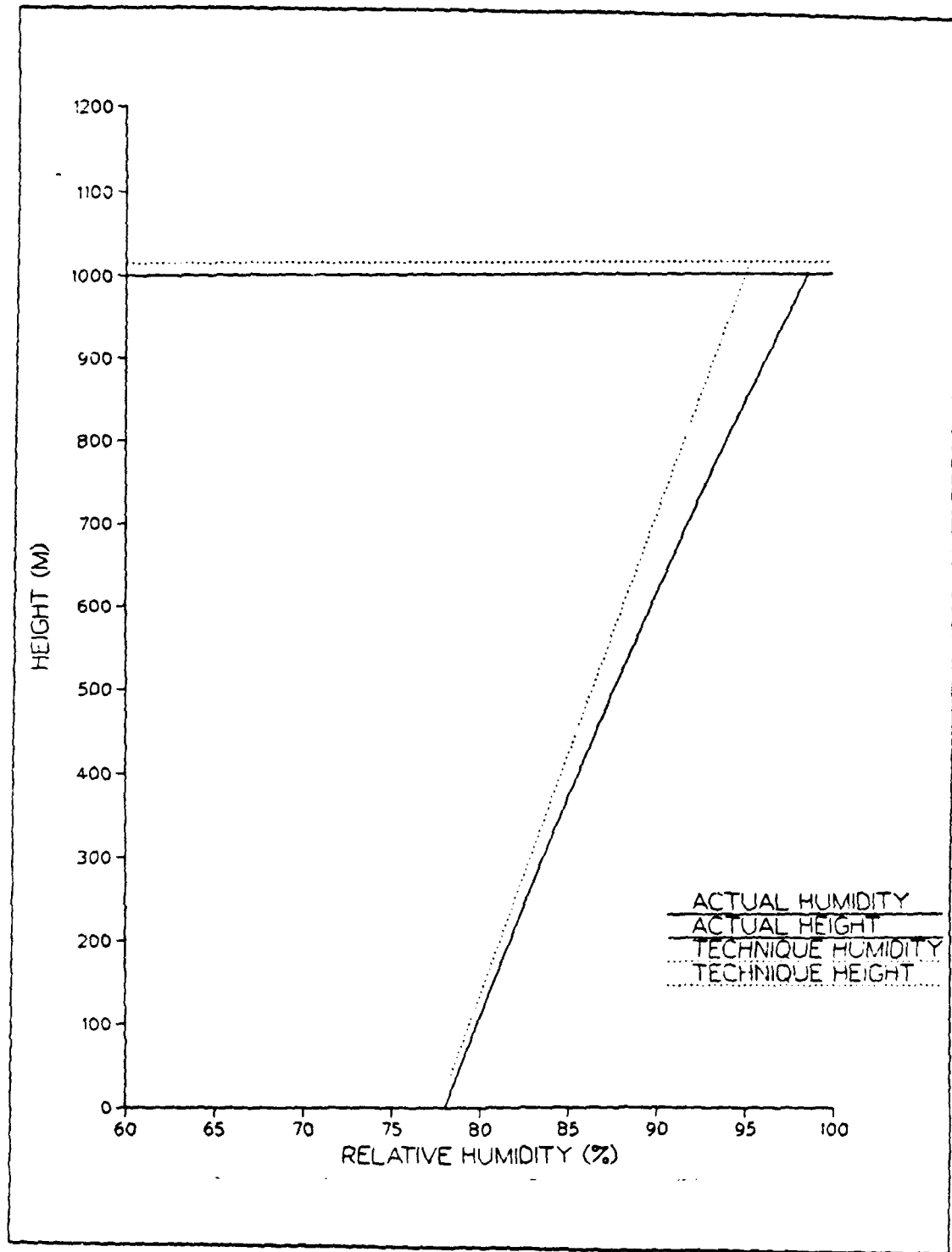


Fig. 4.5 Model and technique produced MABL depths and humidities.
Model surface humidity = 78%.

C. TECHNIQUE SYSTEMATIC ERRORS

The estimated versus actual model comparisons suggest two tendencies which were verified by additional model testing. The first tendency was seen in the effect of variations in model depth on the technique's performance. The technique systematically converges to higher relative humidities and lower depths for model layers in excess of 750 m. The second tendency was for the estimated humidity profile to exceed the model humidity profile for surface humidities less than 70%, and to decrease, becoming less than the model profile for surface humidities greater than 70%.

Table 2 indicates the percentage deviation of technique layer depth from model values for the three layer depths. A growing deviation between the model and technique estimated depth results for deeper boundary layers. The technique begins to underestimate layer depth for layers deeper than about 750 m. The observed systematic error with various MABL depths results primarily from the choice of a linear parameterization of relative humidity with height. Figs. 4.1 to 4.3 help illustrate the impact of this parameterization. For shallow MABLs, curvature in the actual relative humidity profile is minimal. With increasing depth, curvature becomes increasingly important, and the linear profile becomes less valid. Curvature of the model profile occurs because of the nonlinear relationship between temperature and saturation vapor density (See Fig. 2.10). The linear vertical temperature profile translates into a nonlinear saturation vapor density profile. From Eq. 2.20, the formulation of relative humidity depends on the ratio between vapor density and saturation vapor density. Fig. 3.3 shows that vapor density varies linearly with height in the well-mixed MABL. Therefore, the nonlinearity in saturation vapor density with height causes relative humidity as a function of height to vary nonlinearly. The nature of the relative humidity profile curvature is seen in Fig. 4.2. For deeper boundary layers (in excess of 750 m), the technique parameterization of humidity leads to generally higher humidities at all levels, which result in higher extinction values. For a fixed, measured optical depth, a higher integrated value of extinction leads to a reduced estimate of MABL depth.

The second systematic tendency is associated with the choice of the variable C . This variable not only represents changes in the slope of the relative humidity profile with changing layer depths, but is also a function of surface relative humidity. The departure of the estimated humidity profile from the model's profile occurs around a surface humidity value of 70% since the equation utilized by the technique to compute the value of C (Eq. 3.9) was based on $RH(0) = 70\%$.

TABLE 2
DEVIATION BETWEEN TECHNIQUE AND MODEL LAYER DEPTH

	500	1000	1500
Error in layer depth	+0.6%	-0.5%	-2.0%

The dependence on surface humidity can be illustrated through the ratio of vapor density to saturation vapor density in the relative humidity definition. Fig. 4.6 shows the vapor density varying linearly with height in the model MABL. A change in surface humidity causes the vapor density curve to shift. Saturation vapor density undergoes a nonlinear decrease with height (temperature). The effect of a shift in the vapor density curve has a greater percentage impact on the upper portion of the layer than the lower portion, in terms of a change in humidity. Hence, the change in relative humidity from the bottom to the top of the profile is dependent on the surface humidity. The dependency is nonlinear, and increases more rapidly for higher surface humidities. Since saturation vapor density as a function of temperature also changes nonlinearly, the vertical slope in relative humidity is also apparently a function of temperature.

D. RELATIONSHIP BETWEEN SURFACE RELATIVE HUMIDITY AND MABL DEPTH

The link between surface relative humidity and MABL depth can be explained physically and illustrated by an example. The change in surface relative humidity is translated directly through the depth of the MABL since the slope of the technique parameterized humidity profile is fixed. Therefore, an increase in surface humidity leads to an increase in humidity for the layer. The increase in layer humidity results in an increase in layer extinction. Since optical depth is a fixed measured quantity, the increase in extinction through higher layer humidities results in a reduced estimate of MABL depth by the technique.

An alternative explanation can also be given. An increase in layer humidity, provided temperature is constant, is equivalent to an increase in moisture. Since the amount of water vapor is fixed by measurement, the layer depth in which it is contained must decrease because of the increase in moisture. The relationship between

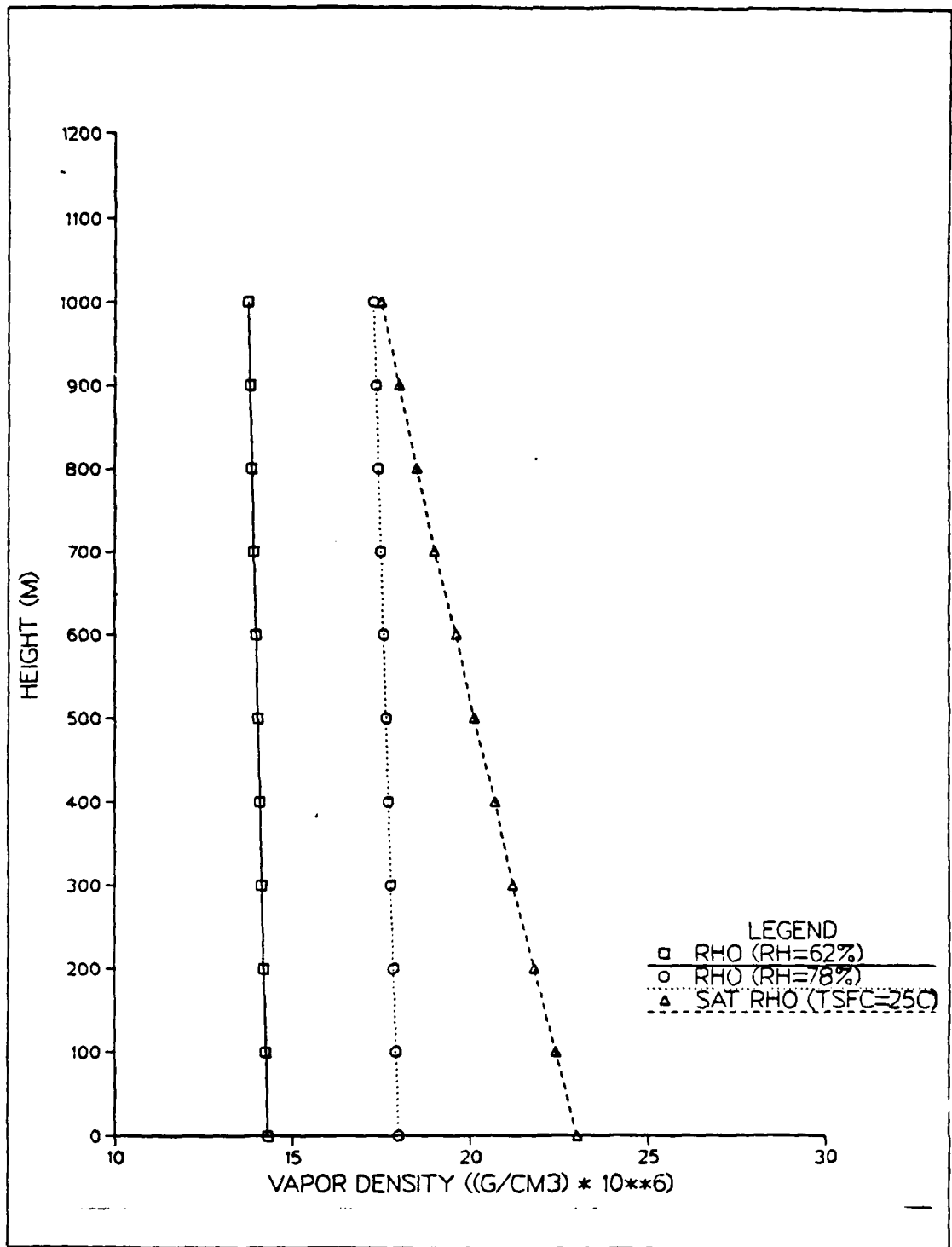


Fig. 4.6 Vapor density for $RH(0) = 62\%$ (solid) and $RH(0) = 78\%$ (dotted) compared to the saturation vapor density profile based on $T_{sfc} = 25^\circ\text{C}$.

technique determined surface humidity and MABL depth can be summarized as follows. An increase (decrease) in surface humidity brings about a decrease (increase) in MABL depth.

V. SENSITIVITY TO UNCERTAINTY IN MEASUREMENTS

Potentially, the most significant source of error in the relative humidity and depth estimates arises from inaccuracies in the measurement of the input quantities of water vapor, optical depth, sea surface temperature and sea level pressure. This chapter investigates the effect of uncertainties in the input variables on the determination of surface relative humidity and MABL depth. This type of analysis isolates the variables which must be most accurately specified. Also in this chapter, the link between each variable and the output of surface relative humidity is discussed.

A. RESULTS OF SENSITIVITY STUDIES

Technique sensitivity is the response of the method to the perturbation of an input quantity. The response is measured as the resulting change in the final layer depth. For the sensitivity studies, the amount of input perturbation was limited to the anticipated accuracy of the required remote sensing measurement. The relationships between each variable, and the surface relative humidity are not intuitive, and do not lend themselves to straight forward physical explanation, but may be seen by mathematical arguments. Sensitivity studies for shallow, intermediate and deep MABLs with a surface relative humidity of 70% are conducted.

1. Uncertainty in Observed Water Vapor

Total water vapor (W) was varied about the depth-dependent model values by amounts of ± 0.1 , ± 0.2 and ± 0.5 g/cm². Obviously, the variations constitute a larger percentage of the total water vapor for thinner layers. Consequently, these variations effect the 500 m boundary layer most dramatically.

Table 3 shows the effect of variations in W on the solution for the surface relative humidity and MABL depth. Actual values, on which the perturbations are made, are shown for each model depth. Qualitatively, a comparison with technique retrieved values of surface humidity and layer depth may be made with the results based on the actual value of W . An error in W in excess of the actual value results in a decrease of the surface relative humidity, and an increase in MABL depth. Conversely, an error in W below the actual value cause an increase in surface humidity, and a decrease in MABL depth. The technique encounters difficulties in iterating toward a solution when errors in W of about 25% or greater occur. In these cases, the

technique fails when the measured value exceeds the actual value. For the 500 m thick layer, failure occurs with a variation of $+0.2 \text{ g/cm}^2$. Failure occurs in the 1000 m thick layer when W exceeds the actual value by 0.5 g/cm^2 . Solutions were attained for all variations in W for the 1500 m thick layer.

TABLE 3
EFFECT OF VARIATIONS IN W ON SURFACE HUMIDITY AND
MABL DEPTH

	+0.1	-0.1	+0.2	-0.2	+0.5	-0.5
$z = 500\text{m}$ ($W = 0.799$)						
RH(0)	61.75%	75.65%	-	80.41%	-	91.44%
Δz (m)	635.1	406.5	-	327.5	-	143.0
$z = 1000\text{m}$ ($W = 1.5824$)						
RH(0)	66.56%	73.40%	62.09%	76.21%	-	83.19%
Δz (m)	1109.6	895.6	1246.2	805.9	-	577.9
$z = 1500\text{m}$ ($W = 2.3504$)						
RH(0)	67.98%	73.19%	64.76%	75.38%	48.01%	80.89%
Δz (m)	1582.1	1362.3	1709.2	1273.3	2315.8	1025.9

The link between variations in W and the technique's solution of surface relative humidity can be seen in the quadratic formula solution to Eq 3.6:

$$\text{RH}(0) = \frac{-b \pm \sqrt{b^2 - 4ac}}{2a} \quad (5.1)$$

where

$$\begin{aligned} a &= 1 - (e^{-\tau AC})^2, \\ b &= 2Be^{-\tau AC}(e^{-\tau AC} - 1) \text{ and} \\ c &= B^2(1 - e^{-\tau AC}) + (2.0 \cdot 10^{-3})CW/\rho_{ws}(T = T_{\text{lyr}}). \end{aligned}$$

It has been observed that the meteorologically consistent solution for surface humidity occurs when the positive root of the radical is selected. The only occurrence of W in the quadratic formula for surface relative humidity is in the second term under the radical in Eq. 5.1. An increase in W decreases the term under the radical. This reduces the entire numerator and $RH(0)$ correspondingly decreases. Conversely, a decrease in W translates to an increase in surface humidity.

2. Uncertainty in Observed Optical Depth

Optical depth (τ) was varied by 10, 20 and 50% of its actual value. Table 4 shows the results of these variations on technique derived surface humidity and layer depth. In comparison to model surface humidity and depth values, variations in τ in excess of the actual value cause an increase in surface humidity, and a decrease in layer thickness. An error in τ below the actual value leads to a decrease in surface humidity, and an increase in layer depth. The technique fails for errors in τ which were 50% below the actual values for 500 and 1000 m thick layers.

TABLE 4
EFFECT OF VARIATIONS IN τ ON SURFACE HUMIDITY AND
MABL DEPTH

	+ 10%	-10%	+ 20%	-20%	+ 50%	-50%
$z = 500m$ ($\tau = 0.065$)						
RH(0)	73.54%	64.16%	76.21%	50.46%	81.39%	-
Δz (m)	478.3	544.6	462.2	678.2	433.6	-
$z = 1000m$ ($\tau = 0.168$)						
RH(0)	72.94%	66.41%	74.96%	60.23%	78.80%	-
Δz (m)	962.0	1046.0	938.4	1137.3	896.1	-
$z = 1500m$ ($\tau = 0.549$)						
RH(0)	71.35%	69.86%	71.78%	68.57%	72.47%	57.07%
Δz (m)	1459.0	1485.1	1451.7	1507.9	1440.1	1737.2

The effect of varying τ on surface humidity is difficult to demonstrate from a mathematical standpoint, since it appears as an exponential factor in each term of Eq. 5.1. However, the effect of uncertainties in τ does not have the dramatic impact on estimates of technique layer depth that the W variations produced. This is explained by examining Eq. 2.5, which shows layer thickness in terms of measured optical depth and humidity-dependent extinction. As an example, if τ is perturbed such that it is less than the model value, the surface relative humidity is reduced. This leads to lower relative humidities throughout the MABL and extinction for the layer is reduced. The coincidentally reduced optical depth and layer extinction are related, such that they tend to minimize the error in the estimate of layer thickness.

3. Uncertainty in Observed Sea-Surface Temperatures

Sea-surface temperature (SST) was varied by ± 1 , ± 2 and ± 5 °C. The surface temperature provides the basis for the layer saturation vapor density by Eq. 2.23. Since surface temperature is not a function of layer depth (as are W and τ), a variation is translated equally to each technique solution for the three MABL depths.

Table 5 indicates the effects of variations in SST on the solutions for surface relative humidity and MABL depth. Errors in the temperature above the model values cause surface humidity to increase and layer depth to decrease, whereas the opposite result occurs with errors in temperature below the actual value. In cases where the surface temperature was less than the actual by 5°C, the technique did not converge to a solution.

The response of technique surface humidity to variations in surface temperature can be explained by the same mathematical reasoning as was used earlier to explain W variations. As an example, an increase in SST leads to an increase in layer saturation vapor density. The only occurrence of saturation vapor density in Eq. 5.1 is again in the second term under the radical. As saturation vapor density increases, the term under the radical increases. The numerator increases, so that the surface relative humidity also undergoes an increase.

4. Uncertainty in Observed Sea-Level Pressure

Variations in the estimate of the sea-level pressure do not cause any change in the surface relative humidity, and hence the MABL depth. The estimate is provided to allow calculations with the hypsometric formula and Poisson's equation, to determine the mid-layer temperature. The critical variable here is the layer virtual temperature, which determines layer thickness. The actual values of pressure at the upper and lower boundaries of the layer are inconsequential.

TABLE 5
EFFECT OF VARIATIONS IN SST ON SURFACE HUMIDITY AND
MABL DEPTH

	+1.0°	-1.0°	+2.0°	-2.0°	+5.0°	-5.0°
z = 500m						
RH(0)	72.56%	66.48%	74.86%	62.05%	80.12%	-
Δz (m)	457.6	557.7	419.6	630.2	332.4	-
z = 1000m						
RH(0)	73.04%	66.80%	75.39%	62.37%	80.72%	-
Δz (m)	907.1	1102.2	832.2	1237.8	659.4	-
z = 1500m						
RH(0)	73.89%	66.72%	76.46%	61.21%	82.08%	-
Δz (m)	1337.5	1632.2	1226.1	1845.0	970.2	-

T = 25°C

B. COMPARISON OF ERRORS IN INPUT VALUES

The relative importance of errors in technique input variables to estimated MABL depth is summarized by Fig. 5.1. Each input was varied by the amount of error that is anticipated from the specific measurement technique. W was varied by 0.15 g/cm², τ by 20% and sea-surface temperature by 1°C. These error bars are based on accuracies quoted by Dalu (1986), Griggs (1983) and McClain (1980) respectively. The errors are based on a 1000 m layer. The results indicate that accurate knowledge of W and τ are most critical. In the actual application of this technique, observational errors in all input variables will occur to some extent. A worst case scenario would have each error producing the same effect and the summation of the errors causing an inaccurate or indeterminate surface relative humidity. However, it is most likely that errors in W and τ will tend to counteract, and thereby act to minimize their cumulative effects. This occurs because of the original assumptions of water vapor and optical

depth being confined to the boundary layer. In actuality, some of each quantity will be present above the layer. From Tables 3 and 4, overestimates of each quantity will have compensating effects on the technique estimate of surface relative humidity and layer depth.

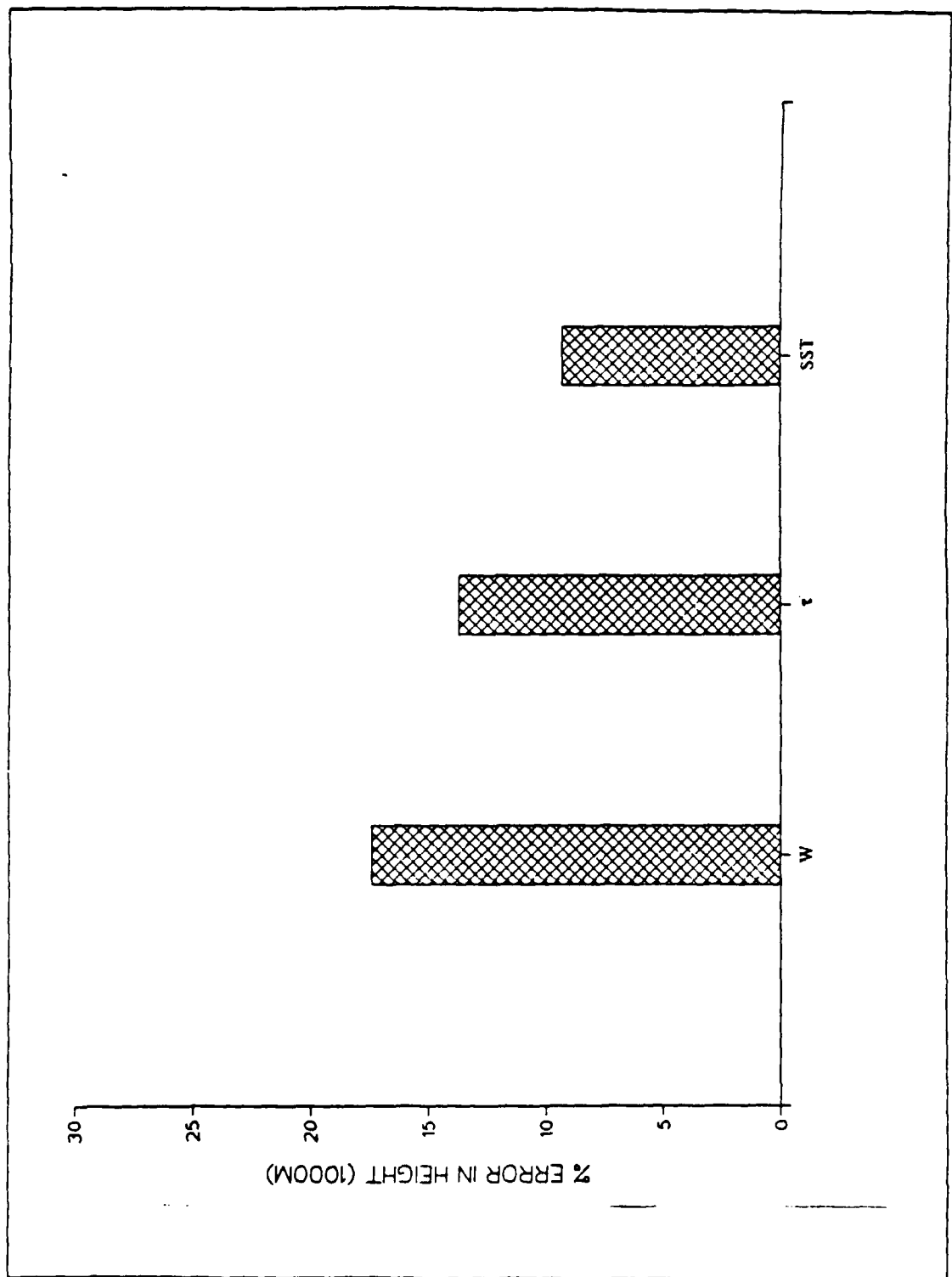


Fig. 5.1 Effect of input errors on technique MABL depth.

VI. CONCLUSIONS AND RECOMMENDATIONS

A technique for determining MABL depth and relative humidity structure was presented. The technique relies solely on remotely sensed values of aerosol optical depth, total water vapor and sea-surface temperature. The remote measurements are multispectral, employing channels 1, 4 and 5 of NOAA's Advanced Very High Resolution Radiometer (AVHRR) instrument. This initial developmental study has shown:

- In theory, estimations of MABL depth and relative humidity profiles can be done remotely.
- Some treatment of the vertical variation of relative humidity with height is necessary. A linear parameterization of the relative humidity profile is effective in accounting for the nonlinearity in the relationship between extinction and higher values of relative humidity.
- The technique is most sensitive to expected errors in total water vapor measurements, and to a lesser extent errors in optical depth and sea-surface temperature measurements.

Since this study introduces an original and unconventional method, a significant amount of effort remains to improve, test and validate the technique.

Recommendations for future work include:

- Develop the treatment of the vertical relative humidity profile to account for the slope of the relative humidity profile due to changes in the surface humidity and layer temperature, as well as layer depth.
- Study the sensitivity of the technique to variations in the extinction - relative humidity relationship.
- Improve the mixed layer sophistication to include variations in MABL stability and possible surface layer structure.
- Determine to what extent optical depth and water vapor above the boundary layer would produce compensating errors.
- Investigate the technique's performance with actual experimental data sets.
- Give further consideration to the regions of applicability of the technique, possibly limiting it to specific air mass types or introducing air mass dependent modifications.

This study represents a beginning point for the evolution of a method for routinely gathering MABL information from satellite. The large area, high frequency coverage of sun-synchronous satellites may allow the mapping of the MABL. Such

information would allow study of temporal changes in the MABL as well as variations in layer structure with respect to the synoptic-scale environment. Boundary layer mapping would also provide data for dynamic numerical weather prediction model initialization as well as a spatial dimension of duct heights for electromagnetic energy propagation.

LIST OF REFERENCES

- Agarwal, V.K., and A.V. Ashajayanthi, 1983: Boundary Layer Structure over Tropical Oceans from Tiros-N Infrared Sounder Observations. *Journal of Climate and Applied Meteorology*, **22**, 1305 - 1311.
- Bolton, D., 1980: The Computation of Equivalent Potential Temperature. *Monthly Weather Review*, **108**, 1046 - 1053.
- Chesters, D., L. Uccelline and W. Robinson, 1983: Low-Level Water Vapor Fields from the VISSR Atmospheric Sounder (VAS) 'Split Window' Channels. *J. Climate Appl. Meteor.*, **23**, 725 - 743.
- Dalu, G., 1986: Satellite Remote Sensing of Atmospheric Water Vapor. *International Journal of Remote Sensing*, **7**, 1089 - 1097.
- Dalu, G., C. Prabhakara and R. Lo, 1981: Improved Accuracy of the Remote Sensing of Sea Surface Temperature. In *Oceanography from Space*, Edited by J.F.R. Gower, Plenum, New York, 109 - 114.
- Durkee, P.A., 1984: The Relationship Between Marine Aerosol Particles and Satellite-Detected Radiance. Ph.D. Dissertation, Colorado State University, Fort Collins, CO, 124 pp.
- Durkee, P.A., D.R. Jensen, E.E. Hindman and T.H. Vonder Haar, 1986: The Relationship Between Marine Aerosol Particles and Satellite-Detected Radiance. *Journal of Geophysical Research*, **91**, 4063 - 4072.
- Eloranta, E.W., J.M. King and J.A. Weinman, 1975: The Determination of Wind Speed in the Boundary Layer by Monostatic Lidar. *Journal of Applied Meteorology*, **14**, 1485 - 1489.
- Fitzgerald, J.W., 1979: On the Growth of Aerosol Particles with Relative Humidity. NRL memo. report 3847. Naval Research Laboratory, Washington D.C.
- Fitzgerald, J.W., W.A. Hoppel and M.A. Viette, 1982: The Size and Scattering

Coefficient of Urban Aerosol Particles in Washington D.C. as a Function of Relative Humidity. *Journal of Atmospheric Sciences*, **39**, 1838 - 1852.

Gaynor, J.E., and P.A. Mandics, 1978: Analysis of the Tropical Marine Boundary Layer During GATE Using Acoustic Sounder Data. *Monthly Weather Review*, **106**, 223 - 232.

Griggs, M., 1983: Satellite Measurements of Tropospheric Aerosols. *Advances in Space Research*, **2**, 109 - 118.

Hanel, G., 1976: The Properties of Atmospheric Aerosol Particles as Functions of Relative Humidity at Thermodynamic Equilibrium with the Surrounding Moist Air. In *Advances in Geophysics*, **19**, Edited by H.E. Landsberg and J. Van Meighen, Academic Press, New York, 73 - 188.

Koepke, P., and H. Quenzel, 1979: Turbidity of the Atmosphere Determined by Satellite. Calculation of Optimum Viewing Geometry. *Journal of Geophysical Research*, **84**, 7847 - 7856.

Koepke, P., and H. Quenzel, 1981: Turbidity of the Atmosphere Determined by Satellite. Calculation of Optimum Wavelength. *Journal of Geophysical Research*, **86**, 9801 - 9805.

Iqbal, K.N., 1980: *An Introduction to Atmospheric Radiation*. Academic Press, New York, 392 pp.

McClain, P., 1980: Multiple Atmospheric-Window Techniques for Satellite-Derived Sea Surface Temperature. In *Oceanography from Space*, Edited by J.F.R. Cooper. Plenum Press, New York, 77 - 85.

McClain, L.M., and D.S. Crosby, 1984: Theory and Validation of the Multiple Window Sea Surface Temperature Technique. *Journal of Geophysical Research*, **89**, 3655 - 3661.

Nieman, R.A., 1977: A Comparison of Radiosonde Temperature and Humidity Profile Data Bases. CSC TM-77-6133, Contract NAS 5-11999. Computer Sciences Corporation, Silver Spring, MD, 48 pp.

Ortenburger, L.N., S.B. Lawson and G.K. Miller, 1978: Radiosonde data Analysis II. GTE Sylvania, 14 pp.

- Pfeil, F., 1986: Developing a Physical Basis for an Aerosol Climatology of the Pacific Ocean. M.S Thesis, Naval Postgraduate School, Monterey, CA., 75 pp.
- Prabhakara, C., G. Dalu and V. Kunde, 1974: Estimation of Sea-Surface Temperature from Remote Sensing in the 11 to 13 μm Window Region. *Journal of Geophysical Research*, **79**, 5039 - 5044.
- Prabhakara, C., G. Dalu, R.C. Lo and N.R. Nath, 1979: Remote Sensing of Seasonal Distribution of Precipitable Water Vapour over the Oceans and the Inference of Boundary Layer Structure. *Monthly Weather Review*, **107**, 1398 - 1401.
- Prabhakara, C., and G. Dalu, 1980: Passive Remote Sensing of the Water Vapour in the Troposphere and its Meteorological Significance. In *Atmospheric Water Vapor*, Edited by A. Deepak, Academic Press, New York, 355 pp.
- Rogers, R.R., 1979. *A Short Course in Cloud Physics*, Pergamon Press, New York, 235 pp.
- Shettle, E.P., and R.W. Fenn, 1979. Models for the Aerosols of the Lower Atmosphere and the Effects of Humidity Variations on their Optical Properties. AFGL-TR-79-0214 Air Force Geophysics Laboratories, Hanscom AFB, MA, 94 pp.
- Smith, W., and H. Woolf, 1978. Use of Eigenvectors of Statistical Covariance Matrices for Interpreting Satellite Sounding Observations. *Journal of Atmospheric Sciences*, **33**, 1127 - 1140.
- Wendrock, A.H., 1953. Salt Nuclei in Marine Air as a Function of Altitude and Wind Force. *Journal of Meteorology*, **10**, 362 - 371.

INITIAL DISTRIBUTION LIST

		No. Copies
1.	Defense Technical Information Center Cameron Station Alexandria, VA 22304-6145	2
2.	Library, Code 0142 Naval Postgraduate School Monterey, CA 93943-5002	2
3.	Chairman(Code 63Rd) Department of Meteorology Naval Postgraduate School Monterey, CA 93943-5000	1
4.	Chairman(Code 68Tm) Department of Oceanography Naval Postgraduate School Monterey, CA 93943-5000	1
5.	Professor P. A. Durkee(Code 63De) Department of Meteorology Naval Postgraduate School Monterey, CA 93943-5000	6
6.	Professor C. Wash(Code63Wx) Department of Meteorology Naval Postgraduate School Monterey, CA 93943-5000	1
7.	LT Richard J. Kren Naval Oceanographic Command Facility Box 68 FPO Seattle, WA 98762	1
8.	Director Naval Oceanography Division Naval Observatory 34th and Massachusetts Avenue NW Washington, DC 20390	1
9.	Commander Naval Oceanography Command NSTL Station Bay St. Louis, MS 39522	1

- | | | |
|-----|---|---|
| 10. | Commanding Officer
Naval Oceanographic Office
NSTL Station
Bay St. Louis, MS 39552 | 1 |
| 11. | Commanding Officer
Naval Oceanographic Command Facility
Box 68
FPO Seattle, WA 98762 | 1 |
| 12. | Commanding Officer
Fleet Numerical Oceanography Center
Monterey, CA 93943-5000 | 1 |
| 13. | Commanding Officer
Naval Ocean Research and Development Activity
NSTL Station
Bay St. Louis, MS 39522 | 1 |
| 14. | Commanding Officer
Naval Environmental Prediction and Research Facility
Monterey, CA 93943-5000 | 1 |
| 15. | Julie Haggerty
Naval Environmental Prediction and Research Facility
Monterey, CA 93943-5000 | 1 |
| 16. | Chairman, Oceanography Department
U.S. Naval Academy
Annapolis, MD 21402 | 1 |
| 17. | Chief of Naval Research
800 N. Quincy Street
Arlington, VA 22217 | 1 |
| 18. | Office of Naval Research (Code 420)
Naval Ocean Research and Development Activity
800 N. Quincy Street
Arlington, VA 22217 | 1 |
| 19. | Scientific Liason Office
Office of Naval Research
Scripps Institution of Oceanography
La Jolla, CA 92037 | 1 |
| 20. | Mr. Louis J. Kren
6511 Smith Rd.
Brookpark, OH 44142 | 1 |

21. Mr. John Driscoll
12108 Hensel Rd.
Huntley, IL 60142 1
22. Mr. Mike Schoenberger
8231 S. Archer, Apt. 7
Willow Springs, IL 60480 1

END

10-87

DTIC